



## Planned Products of the Mars Structure Service for the InSight Mission to Mars

M. Panning, Ph. Lognonné, W. Bruce Banerdt, R. Garcia, M. Golombek, S. Kedar, B. Knapmeyer, A. Mocquet, Nick A. Teanby, J. Tromp, et al.

### ► To cite this version:

M. Panning, Ph. Lognonné, W. Bruce Banerdt, R. Garcia, M. Golombek, et al.. Planned Products of the Mars Structure Service for the InSight Mission to Mars. *Space Science Reviews*, 2017, 211 (1-4), pp.611-650. 10.1007/s11214-016-0317-5 . hal-01534998

HAL Id: hal-01534998

<https://hal.science/hal-01534998>

Submitted on 23 Jan 2019

**HAL** is a multi-disciplinary open access archive for the deposit and dissemination of scientific research documents, whether they are published or not. The documents may come from teaching and research institutions in France or abroad, or from public or private research centers.

L'archive ouverte pluridisciplinaire **HAL**, est destinée au dépôt et à la diffusion de documents scientifiques de niveau recherche, publiés ou non, émanant des établissements d'enseignement et de recherche français ou étrangers, des laboratoires publics ou privés.



## Open Archive Toulouse Archive Ouverte (OATAO)

OATAO is an open access repository that collects the work of some Toulouse researchers and makes it freely available over the web where possible.

This is an author's version published in: <https://oatao.univ-toulouse.fr/21703>

**Official URL:** <https://doi.org/10.1007/s11214-016-0317-5>

### To cite this version :

Panning, Mark P. and Lognonné, Philippe and Bruce Banerdt, W.,... [et al.] Planned Products of the Mars Structure Service for the InSight Mission to Mars. (2017) Space Science Reviews, 211 (1-4). 611-650. ISSN 0038-6308

# Planned Products of the Mars Structure Service for the InSight Mission to Mars

Mark P. Panning<sup>1</sup> · Philippe Lognonné<sup>2</sup> · W. Bruce Banerdt<sup>3</sup> · Raphaël Garcia<sup>4</sup> ·  
Matthew Golombek<sup>3</sup> · Sharon Kedar<sup>3</sup> · Brigitte Knapmeyer-Endrun<sup>5</sup> ·  
Antoine Mocquet<sup>6</sup> · Nick A. Teanby<sup>7</sup> · Jeroen Tromp<sup>8</sup> · Renee Weber<sup>9</sup> · Eric Beucler<sup>6</sup> ·  
Jean-Francois Blanchette-Guertin<sup>2</sup> · Ebru Bozdag<sup>10</sup> · Mélanie Drilleau<sup>2</sup> ·  
Tamara Gudkova<sup>11,12</sup> · Stefanie Hempel<sup>4</sup> · Amir Khan<sup>13</sup> · Vedran Lekić<sup>14</sup> ·  
Naomi Murdoch<sup>4</sup> · Ana-Catalina Plesa<sup>15</sup> · Attilio Rivoldini<sup>16</sup> · Nicholas Schmerr<sup>14</sup> ·  
Youyi Ruan<sup>8</sup> · Olivier Verhoeven<sup>6</sup> · Chao Gao<sup>14</sup> · Ulrich Christensen<sup>5</sup> · John Clinton<sup>17</sup> ·  
Veronique Dehant<sup>16</sup> · Domenico Giardini<sup>13</sup> · David Mimoun<sup>4</sup> · W. Thomas Pike<sup>18</sup> ·  
Sue Smrekar<sup>3</sup> · Mark Wieczorek<sup>2</sup> · Martin Knapmeyer<sup>15</sup> · James Wookey<sup>7</sup>

**Abstract** The InSight lander will deliver geophysical instruments to Mars in 2018, including seismometers installed directly on the surface (Seismic Experiment for Interior Struc-

---

✉ M.P. Panning  
[mpanning@ufl.edu](mailto:mpanning@ufl.edu)

<sup>1</sup> Department of Geological Sciences, University of Florida, 241 Williamson Hall, Box 112120, Gainesville, FL 32611, United States

<sup>2</sup> Institut de Physique du Globe de Paris, Univ Paris Diderot-Sorbonne Paris Cité, 35 rue Hélène Brion—Case 7071, Lamarck A—75205 Paris Cedex 13, France

<sup>3</sup> Jet Propulsion Laboratory, California Institute of Technology, 4800 Oak Grove Drive, Pasadena, CA 91109, United States

<sup>4</sup> Institut Supérieur de l’Aéronautique et de l’Espace, Toulouse, France

<sup>5</sup> Max Planck Institute for Solar System Research, Justus-von-Liebig-Weg 3, 37077 Göttingen, Germany

<sup>6</sup> Faculté des Sciences et Techniques, Laboratoire de Planétologie et Géodynamique, UMR-CNRS 6112, Université de Nantes, 2 rue de la Houssinière—BP 92208, 44322 Nantes Cedex 3, France

<sup>7</sup> School of Earth Sciences, University of Bristol, Wills Memorial Building, Queens Road, Bristol BS8 1RJ, United Kingdom

<sup>8</sup> Department of Geosciences, Princeton University, Princeton, NJ, United States

<sup>9</sup> NASA Marshall Space Flight Center, 320 Sparkman Drive, Huntsville, AL 35805, United States

<sup>10</sup> Géoazur, University of Nice Sophia Antipolis, 250 rue Albert Einstein, 06560 Valbonne, France

<sup>11</sup> Schmidt Institute of Physics of the Earth, Russian Academy of Sciences, B. Gruzinskaya, 10, Moscow 123495, Russia

<sup>12</sup> Moscow Institute of Physics and Technology (MIPT), Institutsky per., 9, Moscow region, 141700, Russia

ture, SEIS). Routine operations will be split into two services, the Mars Structure Service (MSS) and Marsquake Service (MQS), which will be responsible, respectively, for defining the structure models and seismicity catalogs from the mission. The MSS will deliver a series of products before the landing, during the operations, and finally to the Planetary Data System (PDS) archive. Prior to the mission, we assembled a suite of *a priori* models of Mars, based on estimates of bulk composition and thermal profiles. Initial models during the mission will rely on modeling surface waves and impact-generated body waves independent of prior knowledge of structure. Later modeling will include simultaneous inversion of seismic observations for source and structural parameters. We use Bayesian inversion techniques to obtain robust probability distribution functions of interior structure parameters. Shallow structure will be characterized using the hammering of the heatflow probe mole, as well as measurements of surface wave ellipticity. Crustal scale structure will be constrained by measurements of receiver function and broadband Rayleigh wave ellipticity measurements. Core interacting body wave phases should be observable above modeled martian noise levels, allowing us to constrain deep structure. Normal modes of Mars should also be observable and can be used to estimate the globally averaged 1D structure, while combination with results from the InSight radio science mission and orbital observations will allow for constraint of deeper structure.

**Keywords** Mars · Seismology · Interior structure · InSight mission

## 1 Introduction

In order to obtain detailed information on planetary interiors, surface geophysical observations in general, and seismological measurements in particular are of critical importance (e.g. Lognonné and Johnson 2007). Much of our knowledge of the internal structure of the planetary bodies in our solar system is achieved through observations such as gravity field, rotation, and tides obtained by precisely tracking orbiting spacecraft or landers on the planets surface, but those observations provide an integrated view of interiors which is generally non-unique. For the Earth, on the other hand, we have a detailed picture of the interior primarily obtained through the study of seismic data.

Prior to the first recording of global scale seismograms by Von Rebeur-Paschwitz (Von Rebeur-Paschwitz 1889), the best information on the Earth's internal structure was determined from Earth tide analysis (Thomson 1863; Darwin 1882). After the advent of quality seismometers in the late 19th and early 20th centuries, our knowledge of Earth structure expanded rapidly with the discovery of the core by Richard Oldham in 1906, the crust-mantle discontinuity by Andrija Mohorovičić in 1909, and the inner core by Inge Lehmann in 1936. By 1939, Harold Jeffreys had produced a 1D global model of the whole Earth capable of matching P wave arrivals within 0.2 % (see e.g. Lay and Wallace 1995, ch. 1). The only other

<sup>13</sup> Institut für Geophysik, ETH Zürich, 8092 Zürich, Switzerland

<sup>14</sup> Department of Geology, University of Maryland, College Park, MD 20742, United States

<sup>15</sup> German Aerospace Center (DLR), Rutherfordstrasse 2, 12489 Berlin, Germany

<sup>16</sup> Royal Observatory Belgium, Av Circulaire 3-Ringlaan 3, 1180 Brussels, Belgium

<sup>17</sup> Swiss Seismological Service, ETH Zürich, 8092 Zürich, Switzerland

<sup>18</sup> Department of Electrical and Electronic Engineering, Imperial College, London, United Kingdom

planetary body, however, for which we have obtained seismic data unambiguously containing signals from the interior is the Earth's moon. The data from seismometers deployed on the Moon as part of Apollo Passive Seismic Experiment by astronauts in five of the six Apollo missions between 1969 and 1972, which recorded data until 1977, gave first order constraints on lunar interior structure, while also producing very unexpected seismograms showing high levels of scattering (e.g. Nakamura 1983). Perhaps the best illustration of the power of such scarce planetary seismic data is the number of studies in recent years based on the Apollo data that have continued to update our understanding of the lunar interior, including observations of the core and possible deep partial melt, despite not receiving any new data since the 70's (Khan and Mosegaard 2002; Lognonné et al. 2003; Chenet et al. 2006; Gagnepain-Beyneix et al. 2006; Khan et al. 2007; Weber et al. 2011; Garcia et al. 2011; Zhao et al. 2012; Steinberger et al. 2015; Matsumoto et al. 2015).

The planned InSight lander mission to Mars (Banerdt et al. 2013) will extend planetary seismology to Mars, and enable other surface geophysical measurements to determine details of the internal structure and evolution of another terrestrial planet for the first time. The mission will include 3-component broadband and short period seismometers (Seismic Experiment for Interior Structure, SEIS, Lognonné et al. 2012; Mimoun et al. 2012; Lognonné and Pike 2015), as well as a heat flow probe (Heat flow and Physical Properties Probe, HP<sup>3</sup>, Spohn et al. 2014), a geodetic experiment (Rotation and Interior Structure Experiment, RISE, Folkner et al. 2012), and a magnetometer, in addition to meteorological sensors.

While 2 seismometers were landed on Mars during the Viking missions in the late 1970's, the seismometer on Viking 1 did not properly uncage, and the placement of the seismometer on the top of the Viking 2 lander prevented the recovery of any signals definitively originating in the planetary interior (Anderson et al. 1977). Twenty years later, a second unsuccessful attempt was made with the OPTIMISM seismometers (Lognonné et al. 1998) onboard 2 Small Autonomous Stations (Linkin et al. 1998) of the failed Mars96 mission. The placement of the sensitive SEIS instrument package directly on the surface of Mars by the InSight lander, however, is likely to usher in a new era of planetary seismology, enabling broadband seismology and the recording of seismic and gravimetric signals from tidal frequencies up to high frequency seismic waves at 50 Hz.

The primary science deliverables from the SEIS instrument are internal structure models of Mars and a seismicity catalog defining activity on Mars. To that end, the SEIS team has formed two main services for the mission: the Mars Structure Service (MSS) to focus on defining the internal structure models and the Marsquake Service (MQS) to catalog the detected marsquakes and impacts. While the two tasks are intimately related and will require constant feedback and interaction, these two services provide a structure to ensure the mission will meet its science goals. In this paper, we describe the major anticipated products of the MSS starting from pre-launch models through initial modeling and refinement as more data becomes available through the nominal 2 year duration of the mission. This is meant primarily to serve as a high level overview and summary of the published and ongoing research being done on these topics by researchers within the MSS, and more detailed descriptions can be found for most techniques and products in the included references. In the following sections, we detail the products already produced and planned in advance of the mission (Sect. 2) and anticipated products early in the monitoring phase of the mission (Sect. 3). We then detail the final anticipated products relating to structure from the local shallow subsurface (Sect. 4), crust and shallow mantle (Sect. 5), deep mantle and core (Sect. 6), and planetary scale normal modes and tides (Sect. 7).

**Table 1** Major element composition (weight percent) models

	MAK <sup>a</sup>	DW <sup>b</sup>	LF <sup>c</sup>	EH45 <sup>d</sup>	MM <sup>e</sup>
CaO	5.2	2.4	2.4	2.0	1.9
FeO	15.80	17.9	17.2	17.7	16.9
MgO	29.80	30.2	29.7	27.3	29.1
Al <sub>2</sub> O <sub>3</sub>	6.40	3.0	2.9	2.5	2.5
SiO <sub>2</sub>	41.6	44.4	45.4	47.5	47.1
Na <sub>2</sub> O	0.1	0.5	0.98	1.2	1.2

<sup>a</sup>Morgan and Anders (1979)  
<sup>b</sup>Dreibus and Wänke (1985)  
<sup>c</sup>Lodders and Fegley (1997)  
<sup>d</sup>Sanloup et al. (1999)  
<sup>e</sup>Mohapatra and Murty (2003)

## 2 Pre-Launch Estimates of Structure and Seismicity

Prior to launch, both the MSS and MQS have been active in gathering available *a priori* estimates of martian structure and seismicity. This is an essential process for a variety of reasons. Adequate estimates of sources and structure define our expectations for the types of signals we will recover from the surface of Mars, which is an important input going into the final instrument and lander software design that will be launched. Also, such models are critical inputs to aid in software development for data processing to recover source and structure parameters when real martian data becomes available. Without a doubt, aspects of martian seismograms will present unexpected challenges; nevertheless, the goal of both services is to have mature algorithms and software to handle the incoming data as efficiently as possible.

### 2.1 Structure Estimates

Despite the lack of seismic observational data, basic constraints from planetary mass, moment of inertia, and tidal Love number  $k_2$  (e.g. Genova et al. 2016; Konopliv et al. 2016, for recent estimates), combined with some assumptions on bulk chemistry based on constraints primarily from martian meteorites (McSween 1994; Taylor 2013), allow for several estimates of the internal elastic and compositional structure of Mars (e.g. Mocquet et al. 1996; Sohl and Spohn 1997; Gudkova and Zharkov 2004; Khan and Connolly 2008; Zharkov et al. 2009; Rivoldini et al. 2011).

In preparation for the mission, the InSight science team has developed a suite of consistently calculated *a priori* models to reflect reasonable ranges of initial composition estimates and thermal profiles (Fig. 1). From these, assuming thermodynamic equilibrium, we can calculate seismic properties using first thermodynamics principles with experimentally derived parameters for candidate mantle minerals. A range of different compositions from the literature are used (Table 1), and a hot and cold end member temperature profiles (Fig. 2) computed from thermal evolution models (Plesa et al. 2016). The seismic properties are calculated using the code `Perple_X` (Connolly 2005) with the thermodynamic formulation and parameters of Stixrude and Lithgow-Bertelloni (2011) for the mantle and using the thermodynamical model developed by Rivoldini et al. (2011) for the core. Figure 1 shows the shear wave velocity distribution in the martian mantle calculated for the compositions of Table 1, including 5 different models of martian mantle composition. While no single model is definitive, the suite of derived models can be used in pre-launch testing, and demonstrate the base expectations we have for structure prior to return of actual seismic data from InSight.

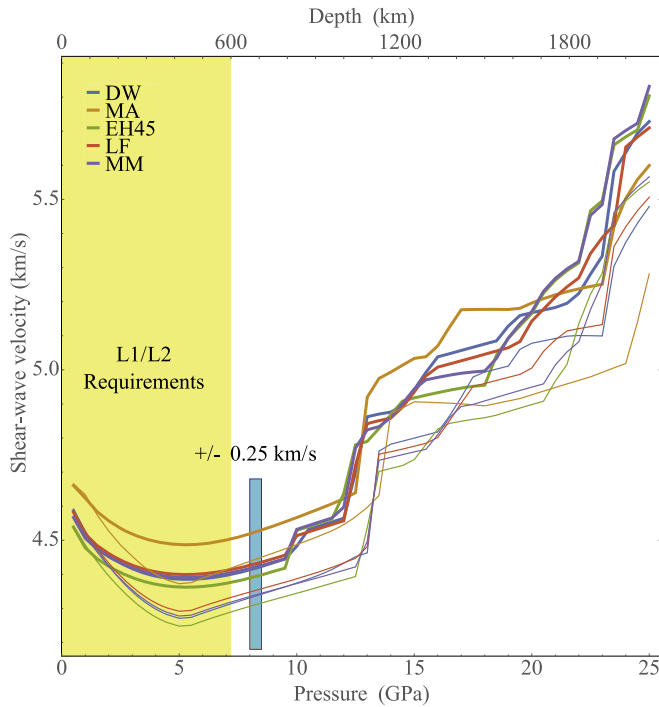


**Fig. 1** A suite of predicted shear wave velocity models for the mantle under Mars conditions for a series of bulk composition models. For each composition, the *thick line* represents calculated properties for a cold thermal profile, while the *thin one* represents a hot profile (Plesa et al. 2016). Temperature profiles are shown in Fig. 2. Composition model abbreviations are defined in Table 1. Light blue colored bar represents the L1 and L2 mission requirements for InSight’s ability to resolve elastic structure. The L1–L2 requirements are defined only for the depth region shaded in yellow

## 2.2 Estimates of Likely Sources

While the seismic catalog will be produced by the other major service of the mission, the MQS, pre-launch estimates of seismicity are also extremely important for defining the techniques that will be useful to determine the structure models. Mars’ seismicity is expected to lie somewhere between that of the Earth and the Moon, with potential sources including faulting, meteorite impacts, and atmospheric hum (Golombek et al. 1992; Lognonné and Mosser 1993; Lognonné et al. 1996; Panning et al. 2015). The Phobos tide is another signal with known amplitude, which can be expected to be detected through stacking (Lognonné and Mosser 1993; Lognonné et al. 2000; Van Hoolst et al. 2003).

The total seismic moment release per year is  $10^{22}$  Nm/yr on the Earth and  $10^{15}$  Nm/yr on the Moon, which loosely brackets the total moment release on Mars to be between  $10^{17}$  Nm/yr and  $10^{19}$  Nm/yr (Golombek 2002). Faulting, driven by internal cooling and large lithospheric loads such as Tharsis, is expected to be the dominant source of seismicity. Estimates based on predicted stress release from internal cooling (Phillips 1991) and the area, total slip and age of surface faults (Golombek et al. 1992) both derive a total moment release for Mars of about  $10^{18}$  Nm/yr. The largest uncertainties in deriving recurrence intervals for different magnitude seismic events center around the assumed negative power law slope of the number versus size of marsquakes and the largest possible marsquake

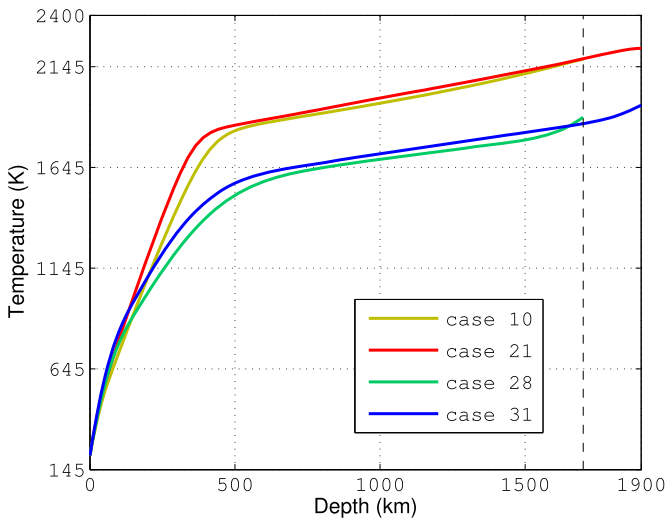


**Fig. 2** Present-day cold and hot end member temperature profiles obtained from thermal evolution models. Case 10 and case 21 from (Plesa et al. 2016) use a reference viscosity of  $10^{21}$  Pa s and a large increase of viscosity with depth (i.e., an activation volume of  $10\text{ cm}^3/\text{mol}$ ) while case 28 and case 31 use a reference viscosity of  $10^{20}$  Pa s and a moderate increase of viscosity with depth (i.e., an activation volume of  $6\text{ cm}^3/\text{mol}$ ). Moreover, case 10 and case 21 have an average crustal thickness of about 45 km, while the cases 28 and 31 use a thicker crust ( $\sim 87$  km) and hence have a mantle more depleted in radiogenic elements. The cases with a mantle thickness of 1700 km (case 10 and case 28) employ two exothermic phase transitions, while for the cases with a mantle thickness of 1900 km an additional endothermic phase transition has been considered. The models of Fig. 1 use the 1900 km profiles. For a detailed description of the thermal evolution models we refer the reader to Plesa et al. (2016)

(Golombek 1994). Knapmeyer et al. (2006) explore these uncertainties and derive a variety of possible models that vary these parameters and bracket the possibilities (Fig. 3). Intermediate estimates suggest  $\sim 100$  marsquakes per year with seismic moments above  $10^{13}$  Nm (detectable at epicentral distance  $\leq 60^\circ$ ).

Of particular interest for InSight are the estimates for seismicity on Cerberus Fossae, one of the youngest tectonic features on Mars from which water carved catastrophic outflow channels (Athabasca Valles to the southwest and Marte Valley to the northeast) (Burr et al. 2002) and lava covered a vast portion of Elysium Planitia (Plescia 1990; Jaeger et al. 2007; Vaucher et al. 2009). Cerberus Fossae has been interpreted as a long graben system with cumulative offsets of 500 m or more (Vetterlein and Roberts 2010), and boulder trails young enough to be preserved in aeolian sediments, indicative of large marsquakes (Roberts et al. 2012), and estimates of moment release that indicate the likelihood of recent marsquakes large enough to be recorded by the InSight instruments (Taylor et al. 2013). Cerberus Fossae is only  $\sim 1500$  km to the east-northeast from the InSight landing site.

Meteorites are expected to be of secondary importance compared to faulting, but have high science potential because accurate locations based on orbital imaging may be possible (Malin et al. 2006; Daubar et al. 2013). Accurate locations would significantly increase the confidence that could be placed on internal structure determinations. Early estimates by Davis (1993) predicted  $\sim 100$  large impacts would be detectable per year with an Apollo-type seismometer. However, subsequent downward revision of the present-day meteoroid source population at Mars (Hartmann 2005) implies that the actual number is likely to be at least an order of magnitude less than this. More recent studies using Hartmann (2005)'s

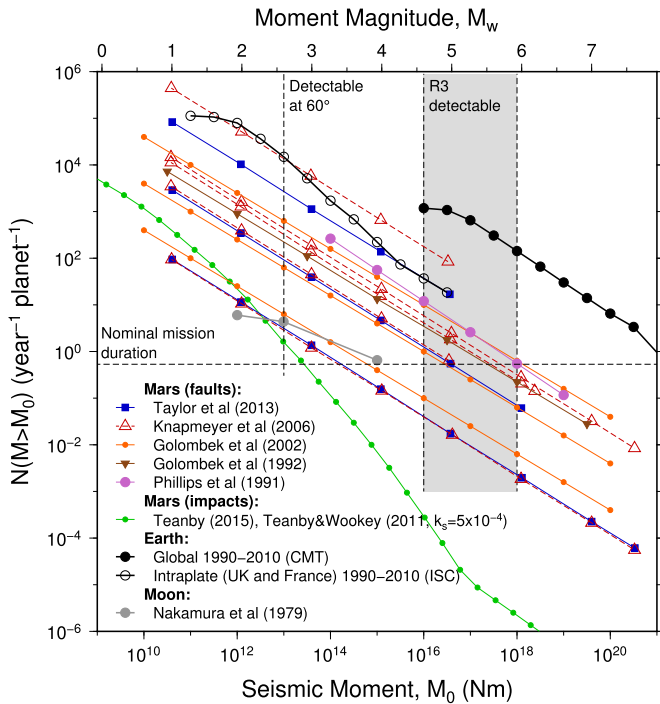


**Fig. 3** Predictions of martian seismicity for faults and impacts. Mars faulting estimates are based on Phillips (1991), Golombek et al. (1992), Golombek (2002), Knapmeyer et al. (2006) (global) and Taylor et al. (2013) (Cerberus Fossae only). Impact seismicity is based on Teanby (2015)'s nominal regional estimates and Teanby and Wookey (2011)'s global estimates with a revised seismic efficiency of  $k = 5 \times 10^{-4}$ . For comparison the seismicity is also shown for the Moon (Nakamura et al. 1979) and Earth (whole globe from Harvard CMT catalogue and Intraplate settings from ISC catalogue). The dashed vertical line shows the threshold magnitude for a detection at  $60^\circ$  offset based on the InSight seismometer performance and waveform modeling (Teanby and Wookey 2011). The grey shaded area shows the threshold magnitude for detection of the R3 surface wave, which will allow source-receiver distance calculations (Panning et al. 2015). Horizontal dashed line indicates mission duration of 1 Mars year (2 Earth years)

updated isochrons, rescaled by a factor of 1/3 to match orbital detection rates of new craters (Malin et al. 2006; Daubar et al. 2013), suggest  $\sim 1$  large globally detectable impact event per Earth year and 0.1–30 regionally detectable events per year (Teanby and Wookey 2011; Teanby 2015) depending on the seismic coupling coefficient. Lognonné and Johnson (2015) propose a rate of about 10 per year with a different approach based on the scaling of the long period seismic energy (e.g.  $< 1$  Hz) with the impact momentum and with estimations of the frequency cutoff based on lunar observations (Lognonné et al. 2009; Gudkova et al. 2015). These estimates contain significant uncertainties, which for impacts are dominated by the large variability of seismic efficiency of the cratering process (Richardson et al. 2005). Fragmentation of small meteoroids (Williams et al. 2014) is another potential source of uncertainty, but is small compared the uncertainties introduced by seismic efficiency (Teanby 2015).

Figure 3 shows the predicted martian seismicity discussed above compared to Earth's measured fault activity from 1990–2010. The global seismicity figures include all sources from the Harvard Centroid Moment Tensor (CMT) event catalogue, which is dominated by

activity at plate boundaries. However, as plate tectonics does not operate on Mars, intra-plate activity (away from plate boundaries, subduction zones, and rifts) may be more representative. Intra-plate events from 1990–2010 in the UK and France are used as a proxy, taken from the International Seismological Centre (ISC) catalogue and converted from local magnitude to seismic moment using the relations in Hanks and Boore (1984). The intra-plate seismicity figures are scaled up to an area equivalent to the Earth’s surface area so as to be comparable with the other estimates.

### 3 Modeling Approach for Initial Velocity Model Delivery

The initial model delivery from MSS is expected to be complete with less than 3 months of data available from the monitoring phase. Therefore, this will need to be a model based on a limited dataset, likely with no more than 1 event large enough to record multiple orbit surface waves, or alternatively a small number of events with body wave phases and first orbit surface wave dispersion identified. When data is limited, modeling approach is very important for understanding the significance of the resulting models. Therefore, we first discuss the Bayesian framework which forms the basis for most of the planned modeling of the MSS. As examples of our proposed approach for developing these initial models, we use a signal from a non-located marsquake combined with signals from a small number of local meteoroid impacts that are located spatially, but not in time (i.e. for which we do not know the time of impact,  $t_0$ ). We first invert for the  $S$ -wave velocity profile using the quake’s Rayleigh wave group velocity dispersion curve (e.g. Panning et al. 2015). We then use the impact data to compute a  $V_P - V_S$  differential velocity profile. These two profiles can then be combined to retrieve a first order  $P$  wave velocity model. Finally, we also discuss modeling events with only the first Rayleigh wave train detected, both with and without considering constraints from mineral physics.

#### 3.1 Inversion Method

We use a Markov chain Monte Carlo (McMC) approach within a Bayesian framework. This approach goes beyond the classical computation of the unique best-fitting solution model (e.g. Mosegaard and Tarantola 1995). This technique allows us to investigate a large range of possible models and provides a quantitative measure of the models uncertainty and non-uniqueness. As such, it is well suited to our problem given the still poorly known nature of the martian interior, as well as the initially low amount of seismic data expected. Bayesian approaches are becoming increasingly popular in planetary studies, in particular for the Moon (Khan et al. 2000; Chenet et al. 2006; Matsumoto et al. 2015), Mars (Khan and Connolly 2008; Rivoldini et al. 2011; Panning et al. 2015; Khan et al. 2016), and Mercury (Rivoldini and Van Hoolst 2013). For planetary applications in particular, the amount of data is likely to be relatively small compared to the Earth, and the forward problem can generally be computed with 1D structure or with relatively fast 3D forward modeling. This allows the computations of several million forward problems with modest processing powers. Such approaches have also become very prevalent in global seismology on the Earth (e.g. Shapiro and Ritzwoller 2002; Khan et al. 2009, 2013; Bodin et al. 2012; Drilleau et al. 2013).

In our test case, the inverse problem consists of computing the  $V_S$  or  $V_P - V_S$  profiles from seismological data (i.e. Rayleigh wave group velocity dispersion diagram or the difference between  $S$  and  $P$  waves’ arrival times). The data  $\mathbf{d}$  are linked to the parameters  $\mathbf{p}$

through the equation  $\mathbf{d} = A(\mathbf{p})$ , where the non-analytic and non-linear operator  $A$  represents the forward problem. In the Bayesian framework, the solutions of the inverse problem are given by the posterior probability  $P(\mathbf{p}|\mathbf{d})$  that the parameters are in a configuration  $\mathbf{p}$  given the data are in a configuration  $\mathbf{d}$ . The parameter space is sampled according to  $P(\mathbf{p}|\mathbf{d})$ . Bayes' theorem links the prior distribution  $P(\mathbf{p})$  and the posterior distribution  $P(\mathbf{p}|\mathbf{d})$ ,

$$P(\mathbf{p}|\mathbf{d}) = \frac{P(\mathbf{d}|\mathbf{p})P(\mathbf{p})}{\sum_{\mathbf{p} \in \mathcal{M}} P(\mathbf{d}|\mathbf{p})P(\mathbf{p})}, \quad (1)$$

where  $\mathcal{M}$  are all the configurations in the parameter space. The probability distribution  $P(\mathbf{d}|\mathbf{p})$  is a function of the misfit, which estimates the difference between the observed data  $\mathbf{d}$  and the computed synthetic data  $A(\mathbf{p})$ . To calculate the posterior distribution (Eq. (1)), we use the Metropolis algorithm (e.g. Metropolis et al. 1953; Hastings 1970), which relies on a randomized decision rule that accepts or rejects the proposed model according to their fit to the data and the prior. This algorithm samples the model space with a sampling density proportional to the unknown posterior probability density function (PDF).

The Markov chain Monte Carlo algorithm that we use is presented in Drilleau et al. (2013) and Panning et al. (2015). The reader is referred to these papers for further details on the practical implementation of the method. The parameterization of the  $V_S$  and  $V_P - V_S$  profiles is done with Bézier points, also known as control points (Bézier 1966, 1967). The points are interpolated with  $C^1$  Bézier curves. The advantage of such a parameterization is that it relies on a small number parameters that do not need to be regularly spaced in depth. Similarly to Panning et al. (2015), we use between 11 and 15 Bézier points to parameterize our mantle velocity models.

We test and apply this method to retrieve a synthetic martian seismic model. This model is derived from the Dreibus-Wänke mineralogy profile (Dreibus and Wänke 1985) using the hot end-member temperature profile, to which we have added a dual-layered crust in order to test our ability to resolve mid-crustal discontinuity structure (dashed lines in Fig. 4). The attenuation profile is taken from Zharkov and Gudkova (1997). The model is considered to be isotropic. In the following sections we detail and present results from the two inversions and the resulting velocity profiles. The synthetic signals used in these inversions were computed with the MINEOS package and correspond to a quake of magnitude 6.0, at  $45^\circ$  epicentral distance, corresponding to a moment of  $10^{18.1}$  Nm. In the next section, we compare results for both a noise-free signal and a noisy signal. The noise is calculated using the complete InSight seismic noise model described in detail in Mimoun et al. (2016). In this model many possible noise sources are considered including contributors due to the mission's instrument itself and to its thermal and magnetic sensitivities, in addition to external contributors such as the mechanical noise originating from the wind-lander interactions (Murdoch et al. 2016b) and the pressure induced ground tilt (Kenda et al. 2016; Murdoch et al. 2016a). Both signals are shown in Fig. 5. Additional work has also been done analyzing coupling of wind noise through the Wind and Thermal Shield (WTS) (Teanby et al. 2016, this issue).

### 3.2 Inversion of Group Velocity Dispersion Diagrams: the S-Wave Velocity Model

Using the McMC method, we invert for the great-circle averaged group velocities of surface Rayleigh waves. Following Panning et al. (2015), if we are able to record up to the 3rd orbit surface waves, the group velocity  $U$  is then

$$U = \frac{2\pi r}{R_3 - R_1}, \quad (2)$$

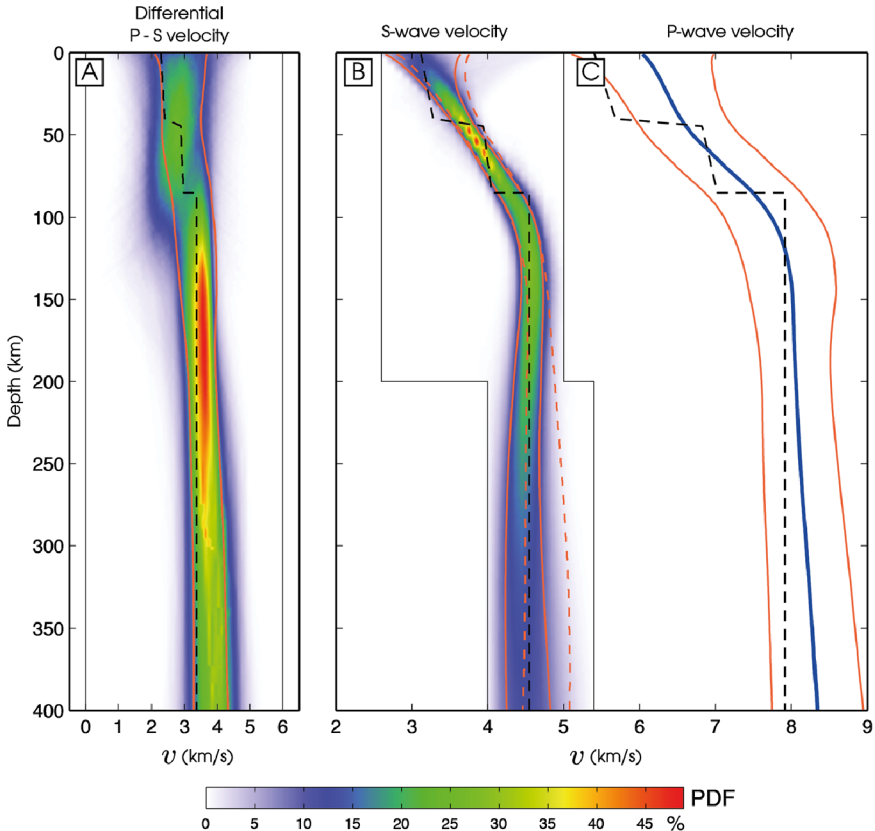


**Fig. 4** Inversion results. The black dashed lines show the model to retrieve. (a) and (b) show *a posteriori* probability density functions (PDF) of differential  $V_P - V_S$  velocity and of S wave velocity. Red and blue colors show high and low probabilities, respectively. Continuous black lines represent the minimum and maximum parameter values allowed. Orange curves delimit the interval between  $\pm 1\sigma$  of the median profile of the distribution.  $S - P$  travel times are used to constraint the differential  $V_P - V_S$  velocity (a), while surface wave dispersion is used to determine  $V_S$  (b). In (b), the orange dashed lines represent the interval between  $\pm 1\sigma$  of the  $V_S$  distribution obtained using the noisy synthetic data. The mean  $V_P$  profile (blue line) in (c) and  $\pm 1\sigma$  standard deviation (in orange) is estimated from the PDFs in (a) and (b)

where  $R1$  and  $R3$  are the arrival times of the first and third orbit of Rayleigh waves, and  $r$  is the planetary radius. Note that  $U$  is independent of the event location such that the event does not need to be precisely located for this method to retrieve a 1-D velocity model.  $U$  can however depend on the azimuth of the surface wave train, as the average group velocity along the great circle linking the event and the station will depend on lateral variations, including ellipticity (Larmat et al. 2008).

Since  $R3$  is not normally easily pickable, due to the dispersion of surface waves and the presence of noise, the measurements of the fundamental mode group velocities correspond to a dispersion diagram (Fig. 6a for noise-free synthetic data, and Fig. 6b for noisy synthetic data). These diagrams are computed (Eq. (2)) using the likelihood of the  $R3$  arrival time in a given frequency band, as defined by the amplitude of the envelope of the seismic waveform in a series of narrow band Gaussian filters. On the plots, for a given frequency, the sum of the probability density of all the group velocities is then equal to one.

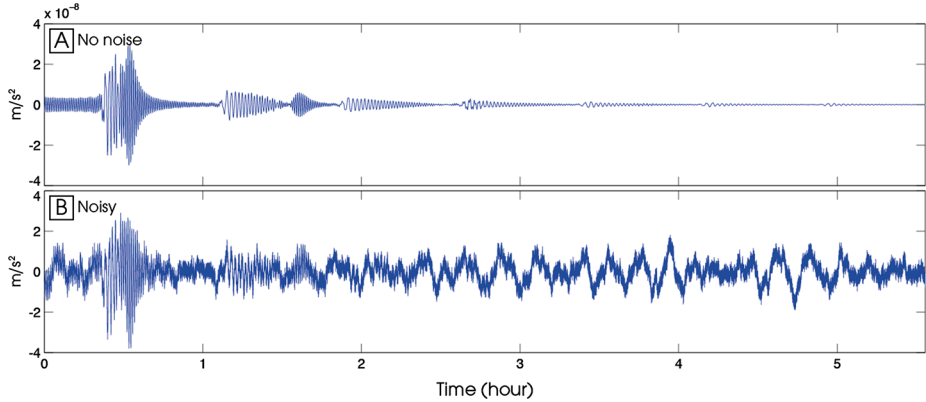


**Fig. 5** Example synthetic seismograms computed using the normal mode code MINEOS (e.g. Woodhouse 1988) with no noise (a) and including the noise model of Mimoun et al. (2016) (b) for a  $M_w 6.0$  event at  $45^\circ$  distance

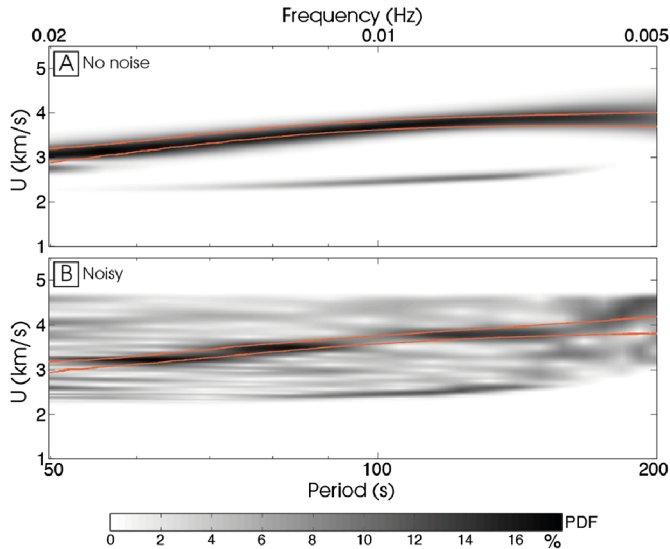


**Fig. 6** Synthetic input dispersion diagrams computed with the seismic model shown in Fig. 4, with no noise (a) and noise (b). The gray scale represents the probability density function assigned to each group velocity value at a given frequency. Black and white show high and low probabilities, respectively. Orange curves circumscribe the predicted group velocity values of all the models accepted by the McMC inversion

In the forward problem, we use the MINEOS software (based on work from Gilbert and Dziewoński 1975 and Woodhouse 1988) to compute the dispersion curves for all sampled models in the 50–180 s period band. These curves are then compared to the data in Fig. 6. The accepted models are combined to retrieve the 1-D  $V_S$  profile PDF averaged along the great circle. The results of the inversions are shown in Figs. 4b and 6. As already demonstrated in Panning et al. (2015), given that only the fundamental mode is considered, the surface waves sensitivity rapidly decreases below 400 km depth and the  $V_S$  distribution is not shown deeper. The  $V_S$  profile is well defined between the surface and 200 km depth,

where the PDF is better constrained. The contours of the dispersion curves associated with the whole set of accepted models are plotted on top of the input dispersion diagrams (Figs. 6a and b). The solution models all produce group velocity dispersion curves that match well with the input data.

The dispersion diagram that results from the noisy synthetic data (Figs. 5 and 6b) shows several maxima for a given frequency, compared to the dispersion diagram from the noise-free synthetic data (Fig. 6a). In Fig. 4b, we plot the  $1\sigma$  standard deviation of the  $V_S$  distributions, for both the noise-free and noisy data (the solid and dashed orange lines, respectively). We observe that the distribution corresponding to the noisy data is shifted by approximately 0.3 km/s at depths greater than 150 km. This is explained by the higher amplitude of low frequencies in the noise spectrum (not shown here). The shift is also observed on the dispersion diagrams (Fig. 6). An important result here is that the  $\pm 1\sigma$  uncertainty around the median of the distribution contains the original input model down to 400 km depth, even with noisy data. We also tested the sensitivity of the results to a higher attenuation model which would decrease the signal to noise ratio. Results (not shown here) indicate that changing the attenuation profile by an order of magnitude does not significantly affect the recovered  $V_S$  distribution.

### 3.3 Inversion of the $V_P - V_S$ Profile

Orbital imagery of the surface near the InSight lander, before and after landing, should provide precise source locations for some of the meteorite impacts recorded by the instruments. However, with no prior knowledge of the seismic velocities in the martian subsurface, the exact time of impact ( $t_0$ ) will be unknown. We outline here and show an example of how we can use these signals to compute a  $V_P - V_S$  differential velocity profile. This new profile can be used to retrieve the  $P$  wave velocity profile when combined with the  $S$  wave velocity profile recovered from the surface wave data.

We use a similar McMC approach as described earlier. If we know the surface location of the source exactly due to orbital imagery, then the only unknown we need in our model is the differential radial  $V_P - V_S$  velocity structure between the impact and the lander. In this case we use a basic ray tracing algorithm (e.g. Shearer 2009) to compute the differential  $S - P$  travel times of the sampled models in the forward problem. We assume that the martian subsurface can be represented with a 1-D velocity model, and that a crust-mantle boundary is present. Therefore, we parameterize the model with two Bezier curves (one in the crust, and one in the mantle), separated by a discrete interface. The depth of that interface is a parameter in the inversion. We limit the range of sampled velocities by setting a minimum  $V_P - V_S$  velocities of 0 km/s (i.e.  $P$  wave velocities must be larger than  $S$  wave velocities) and a maximum differential of 6 km/s, which is in line with proposed martian seismic velocity models (e.g. Dreibus and Wänke 1985; Sohl and Spohn 1997).

We have tested this approach using synthetic data from five impacts with epicentral distance of less than 2000 km. The model used to compute the synthetic travel times is the same as the one used to compute the dispersion curves above (dashed lines in Fig. 4). The maximum depth reached by rays from the furthest event is approximately 400 km. The resulting  $V_P - V_S$  profile is plotted in Fig. 4a. The plot shows a PDF of the accepted differential velocity models. The orange lines indicate the  $\pm 1\sigma$  uncertainty around the median. Overall, we observe a good fit between the recovered and the original model.

One potential drawback of this approach is that it will only be sensitive to the crust-mantle boundary if there is a marked jump in differential  $S - P$  velocities. If the total increase in  $P$  wave velocity is the same as the one in  $S$  wave velocity, then the depth of

interface can not be recovered. In this test case, we have recovered the jump in differential velocities at the base of the crust (at around 80 km) but we are not as sensitive to the mid-crustal interface (near 50 km). As the change in relative velocity across the Moho is small, the recovered contrast is small, even though it is resolved at the correct depth. Better recovery of the Moho and internal discontinuities requires the inclusion of receiver functions as discussed in Sect. 5.

By combining the velocity profiles from the inversion work above, we can recover a first-order  $P$  wave velocity profile (shown in Fig. 4c). The mean of the profile (dark blue line) is the sum of the means of the  $V_S$  and  $V_P - V_S$  profiles, whereas the standard deviation ( $\pm 1\sigma$  uncertainty around the mean shown by the orange lines) is the square root of the sum of the variances from both profiles. With the exception of a small depth range immediately above the unrecovered mid-crustal interface, the recovered profile matches well with the initial synthetic model within the  $1\sigma$  uncertainty.

### 3.4 Modeling Events Without Observations of Higher Orbit Surface Waves

In the previous section, we took advantage of particular data types that allow us to move forward without strong prior constraints on the velocity model. For higher-orbit surface waves (i.e. surface waves which propagate to the station either along the major arc between source and receiver or including multiple orbits of the planet), the known geometry of the planet allows us to constrain the velocity measurements of multiple-orbit surface waves even without an estimated location. For the impact data, the location is constrained by orbital imagery instead. However, we will also likely record many events that are smaller, but still allow us to make clear measurements of  $P$  and  $S$  arrivals and a dispersed first orbit surface wave, even if they are not big enough to record higher-orbit surface waves. For these events, we need to perform simultaneous inversions for both event and structural parameters. A Bayesian approach like the McMC method described above is once again a reasonable method for proceeding in this case.

#### 3.4.1 Inversion Using a Priori Information from Mineral Physics

One powerful technique to allow the development of tight constraints on velocity structure with a relatively limited initial dataset is to use Bayesian techniques informed by strong priors defined by thermodynamic mineral physics models (Khan et al. 2016). In this approach, we invert simultaneously for location and structural parameters following the approach of Khan and Connolly (2008).

As a demonstration of the potential for using this approach, we calculated synthetic seismograms for an *a priori* martian model. This model was calculated with a major element composition as defined by Dreibus and Wänke (1985) and a temperature profile equivalent to the “hot” profile of Verhoeven et al. (2005) with a lithospheric thickness of 300 km. The mineral phase assemblages and resulting seismic velocities are determined following the approach of Khan and Connolly (2008), while the anelastic structure is defined following the approach of Nimmo and Faul (2013) with an assumed grain size of 1 cm.

Based on this radial model, synthetic martian seismograms for two events were calculated using the numerical wave propagation code AxiSEM (Nissen-Meyer et al. 2014), including a realistic noise model (Murdoch et al. 2015), although we used a constant Q model for computational reasons, which neglected the full frequency dependence of Q from the attenuation model of Nimmo and Faul (2013). The two events included a large  $M_W 5.1$  event at  $86.6^\circ$  from the station and a smaller  $M_W 3.8$  event at a closer distance of  $27.6^\circ$ .

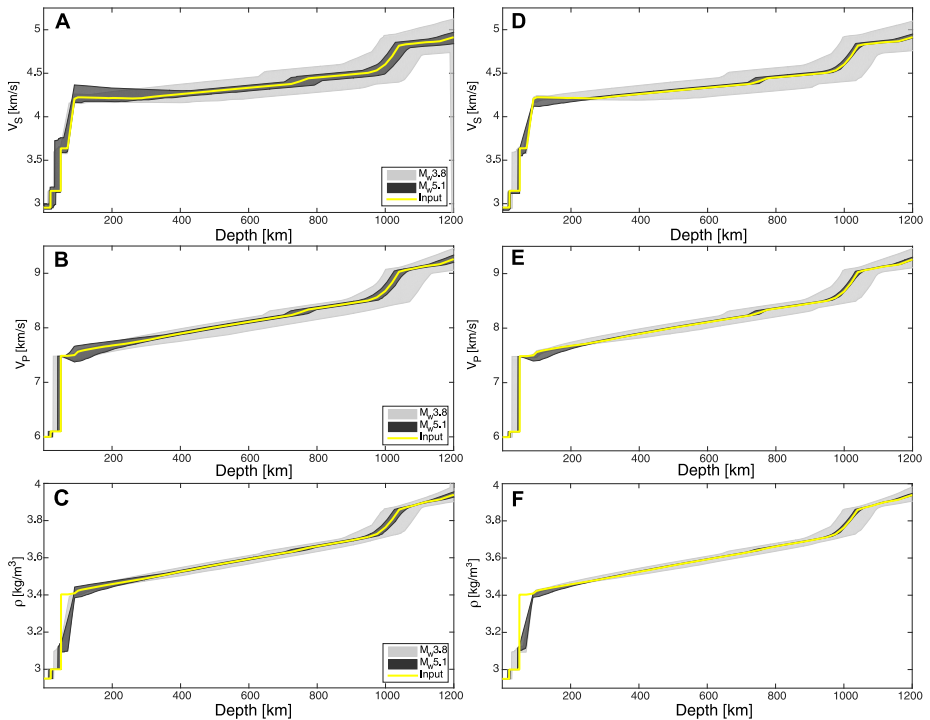


**Fig. 7** “Preliminary” ((a)–(c)) and “Final” ((d)–(f)) inverted martian models. Shown are profiles of  $S$ -wave speed ((a), (d)),  $P$ -wave speed ((b), (e)), and density ((c), (f)). Envelopes encompass all sampled models. Input designates the input model employed for computing martian seismograms. “Preliminary” inverted models are based on dispersion and  $P$ - and  $S$ -wave travel time data. “Final” inverted models are based on dispersion and the expanded travel time data set. The  $M_w 5.1$  event is located at an epicentral distance of  $86.6^\circ$  as a result of which rays sample deeper than in the case of the regional  $M_w 3.8$  event ( $27.6^\circ$ ). Figure from Khan et al. (2016)

To verify the simultaneous location and structure determination, observations of Rayleigh wave dispersion and arrival times of  $P$  and  $S$  waves were picked from the synthetic seismograms. The modeling of source and structure parameters proceeds for each event individually using a Bayesian approach equivalent to the one already described in Sect. 3.1. Rather than having unknown parameters consisting of seismic velocities at a series of Bézier points, however, we instead treat a series of physical parameters as the unknown quantities. In this example, we treat the adiabatic potential temperature, crustal thickness, lithospheric thickness (as defined by the transition from a conductive to adiabatic temperature profile), and core radius as the unknown parameters. The composition is currently treated as fixed, but that could also be allowed to vary. Models of seismic structure are generated from these parameters following Connolly (2009), and we produce posterior PDF estimates of  $P$  and  $S$  velocity and density (Figs. 7a–c). These estimates are constrained by  $P$  and  $S$  arrivals and, respectively, 3 orbits of Rayleigh waves for the large event, and the first orbit alone for the smaller event. A density model is included, but it is not directly constrained through the observations, but is instead determined by the *a priori* mineral physics modeling. In the case of the smaller event, deeper structure is also not directly constrained by seismic data, but is instead constrained by the assumed composition and thermal profile consistent with the shallower structure sampled by the event.

Using the model constraints from these “preliminary” models, we then predict arrival times for other body wave phases that propagate through the model, pick these as well and reinvert the expanded dataset in order to produce a “final” model (Figs. 7d–f). In this way, we can produce estimates of martian velocity structure from single or small numbers of events with very well-resolved error estimates.

### 3.4.2 Inversion with Minimal Priors

In any Bayesian inversion, applying tight prior constraints produces lower error estimates on the final model distribution. This is extremely powerful if you have very good prior constraints, as assumed in the previous Sect. 3.4.1. For the synthetic example, which was produced with a model consistent with the mineral physics constraints used in the inversion, relatively small amounts of data allowed for excellent estimation of the final model with relatively small error bars. However, MSS is proceeding with modeling both with and without the prior constraints set by thermodynamically self-consistent mineral physics models of structure.

There are multiple potential reasons to consider Bayesian models with more relaxed prior constraints. Using the mineral physics-based modeling implicitly includes several assumptions. It assumes a known homogenous mantle composition, or at least a range of possible compositions if that part of the model is allowed to vary as well (unlike in the previous section). It assumes the basic character of the temperature profiles are well represented by a variable thickness conductive layer matched to an adiabatic layer specified by a range of potential temperatures. Finally, it assumes the mineral phase assemblage is in thermodynamic equilibrium and that the elastic and anelastic properties of those phase assemblages are well represented by the empirical relationships tuned to laboratory experiments and observations of Earth properties.

None of these assumptions are particularly unrealistic, but there are feasible models that violate one or more of these assumptions. Models of magma ocean solidification produce compositionally stratified models early in Mars history that may resist mixing by thermal convection (e.g. Elkins-Tanton et al. 2003, 2005). Even in the absence of compositional stratification, models derived from seismic data that may sample lateral chemical heterogeneity unevenly may also be best fit by a model that is not consistent with the above assumptions. A relatively cold, conductive lithosphere may also preserve some non-equilibrium phase assemblages. The upper 200 km of the martian mantle also may not be in hydrostatic equilibrium, with possible significant thermal stresses and deviatoric stress supported by plate flexure. Topography/flexure analysis has however shown that the thermal lithosphere was shallower several billions years ago (Belleguic et al. 2005) and since there is no expectation of significant crustal thickening from volcanism in the past 3 billion years growing a depleted mantle layer, it may be reasonable to assume compositional continuity across the current thermally defined lithosphere/asthenosphere boundary.

For this reason, we also test methods to resolve structure using more limited prior constraints using only  $P$  and  $S$  body wave arrivals and observed group velocity dispersion of the first orbit Rayleigh wave between 20 and 250 seconds. Figure 8 shows an example of a Bayesian inversion of synthetic Earth data for 5 events at distances of 500, 1000, 2000, 4000, and 8000 km. While such a broad distribution of epicentral distances may be an optimistic estimate, the frequency range of measurements and small number of events are realistic for an early study, and so this serves as a demonstration of what can be done with minimal prior constraints and a small number of events with excellent data. Models are parameterized as a single layer crust of varying thickness, with a mantle made up of linear gradients and the

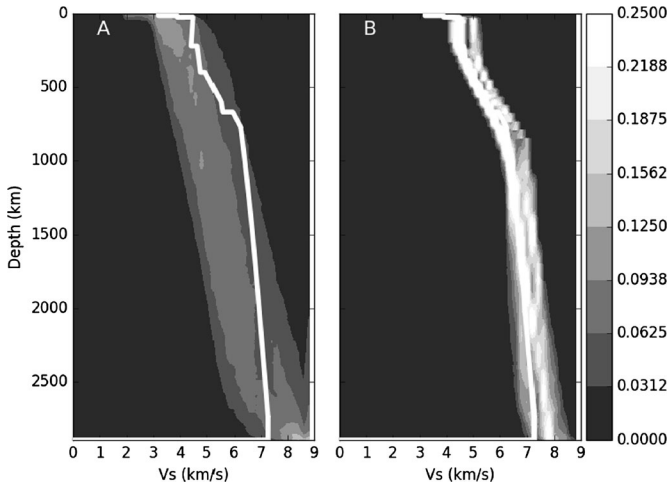


**Fig. 8** Prior (a) and posterior (b) probability density functions for a Bayesian McMC inversion of synthetic Earth data from 5 events between 500 and 8000 km distance. The data were calculated from the model PREM (white line, Dziewonski and Anderson 1981)

mantle  $S$  velocity is allowed to vary within prior bounds with a width of 3 km/s varying linearly from a 3–6 km/s range at the top of the mantle to a 6–9 km/s range at the base of the mantle. Negative gradients are limited to being smaller than 0.005 km/s per km to ensure stability of the travel time calculation, but this needs to be included as low velocity zones in the mantle may be an important feature of the interior of Mars (e.g. Zheng et al. 2015). The number of layers in the mantle is allowed to vary between 2 and 11, with exploration of varying model dimensions accomplished using a type of Bayesian inversion called a trans-dimensional inversion (e.g. Bodin et al. 2012). In order to compare how the different prior constraints affect the final model, we generate a prior distribution simply by running the McMC inversion algorithm without application of acceptance criteria based on data misfit. The limit on negative gradients causes a prior distribution skewed to models with a gradient from minimum to maximum velocity in the mantle rather than a simple uniform distribution (Fig. 8a), but after inversion with the McMC algorithm, the final estimated model PDF shows tight constraints around the true model (shown as white line in Fig. 8b). Multiple events at a variety of epicentral distances were required to obtain similar constraints on the final model distribution as those based on a single event with the mineral physics prior constraints, though. Obtaining similar results from modeling with and without mineral physics prior constraints will allow us to search for possible violations of the mineral physics assumptions, or alternatively to verify that the assumptions are reasonable, permitting us to use the tighter constraints with confidence.

## 4 Local Site Characterization

While a significant focus of the InSight mission is on the structure of the deep interior, geophysical surface observations also provide a unique opportunity to characterize the shallow subsurface at the landing site as well as the crust beneath the landing site. Better characterization of the shallow site response can help in interpreting details of other seismic signals as well as giving a new constraint on geology of the landing site region. In terms of

**Table 2** Subsurface model used to generate synthetic hammer derived seismograms

Thickness (m)	$V_P$ (m/s)	$V_S$ (m/s)	$\rho$ (kg/m <sup>3</sup> )	$Q_P$
50 m	300	173	1500	50
Half-space	2000	1154	2700	100

seismic observations, near-site structure can be best explored using high frequency signals as recorded by the short period SEIS-SP seismometer. We anticipate being able to obtain information using both an active source (hammering by the nearby HP<sup>3</sup> probe) and passive sources (analysis of surface wave amplification obtained from the ambient wavefield). These datasets will be critical since travel times of body waves recorded from distant events also have poor sensitivity to the crustal thickness and constrain only the travel time, i.e. the ratio of the crustal thickness by the seismic velocities. This has been one of the weaknesses of most of the lunar structure crustal inversions, which have provided relatively dispersed crustal thickness estimation despite comparable fits to the travel times. This emphasizes the need for alternative approaches to modeling the shallow structure at the landing site.

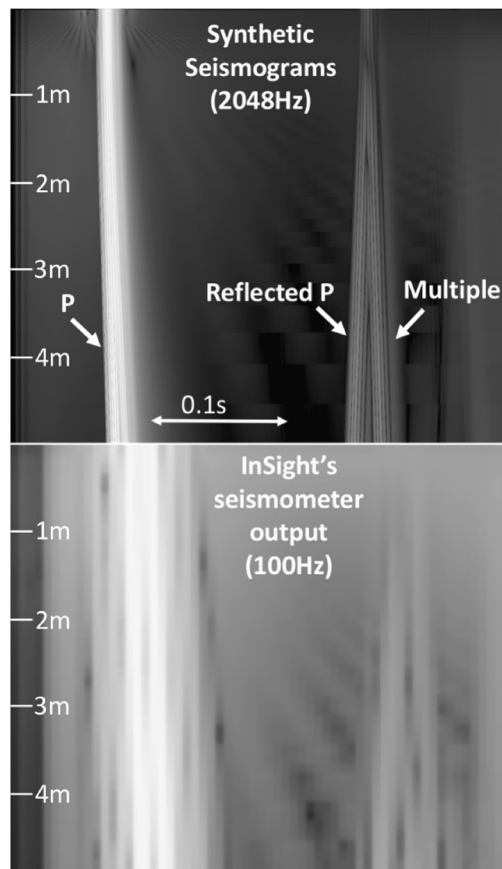
#### 4.1 Analysis of HP<sup>3</sup> Hammering

The HP<sup>3</sup> instrument will be deployed approximately 1–2 m from the surface placement of the SEIS instrument, and is planned to penetrate up to 5 m in depth to measure the heat flow coming from Mars’ interior. The probe, which uses a self-penetration mechanism by an internal hammer and recoil springs, will generate thousands of seismic signals that can be used to analyze the shallow (several tens of meters) subsurface and shed new light on the mechanical properties of martian regolith (Kedar et al. 2016, this issue). The descent will progress in ∼0.5 m hammering intervals, each interval taking between 0.5–4 hours, and each interval being separated by several days of thermal measurements. Each hammering interval consists of several hundred to several thousand strokes ∼3 s apart, depending on the regolith properties. This repeated high frequency active source provides an opportunity to study the shallow structure at the landing site, in particular the thickness and elastic properties of the martian regolith.

As this analysis was not part of the mission threshold objectives, we face some significant challenges to take advantage of this known active source. While the geometry of the SEIS and HP<sup>3</sup> instruments will be very well constrained, we are hampered by the lack of very high frequency sampling (sampling is limited to 100 Hz for both the SEIS-SP and SEIS-VBB sensors) and precise source-sensor timing synchronization, meaning we will not have exact timing of the hammer strokes. In order to better understand how we will be able to use this data, we perform a synthetic test using a simple model of a regolith layer over a half-space (Table 2) to model the high frequency signal and downsample it according to the procedure used by the flight software for SEIS.

Seismograms in this model are calculated using a cartesian geometry mode summation approach (Herrmann 2013) assuming the hammer strokes are sampled at every 1 mm of depth down to the full 5 m of penetration. These 5000 seismograms are displayed in Fig. 9. In this example it is assumed the mole travels vertically downward at a constant rate. In reality, the mole may deviate to some extent from the vertical path. Nevertheless, the mole depth can be calculated from precise distance and tilt measurements taken by the HP<sup>3</sup> system. The distance the HP<sup>3</sup> mole travels is measured to within 4 mm, and its angle to within a degree. In the high frequency output (Fig. 9 top), a direct P wave, a reflected P wave, and a multiple

**Fig. 9** Composite image made of 5000 seismograms at high resolution (*top*, 2048 Hz) and as they would be observed by InSight (*bottom*, 100 Hz). For visual enhancement, each seismic trace is self-normalized against its maximum energy and the color scales based on the logarithm of energy. The lighter appearance of the decimated data (*bottom*) is a manifestation of the smearing of the energy through decimation. At each depth along the vertical axis, the amplitude variation in time along the horizontal axis represents a single seismogram calculated for the hammering at that depth



reflection (representing a wave that propagates up from the hammer and initially bounces off the surface and then the regolith interface before being recorded at the surface) are clearly visible. The relative slopes of these arrivals and their timing constrain the seismic velocity and thickness of the regolith layer. However, we need to simulate a realistic signal, which is both frequency-limited by the sampling of the data, as well as affected by the complex pulse shape of each hammering. This pulse shape has been measured using prototypes of the HP<sup>3</sup> mole device (Kedar et al. 2016, this issue), and consists primarily of two major pulses related to the initial contact of the spring driven hammer followed by the impact of the counter-mass within the mole device a few milliseconds later. The combination of the downsampling and realistic source-time function leads to a smeared seismogram (Fig. 9 bottom). We can still distinguish two arrivals, but the slopes are more difficult to determine, and the reflection and multiple are smeared together. Initial work has shown that the signal can be resampled to higher frequency using sinc interpolation and picks can be made for the direct and reflected wave (Kedar et al. 2016, this issue), however further work involving data stacking and deconvolution of the hammer signal source-time function will likely be necessary for accurate recovery of regolith properties.

## 4.2 Surface Wave Ellipticity

We can also characterize the shallow structure at the landing site by analyzing the response of surface waves recorded at the site. Seismic ground motion experiences significant amplification, especially in horizontal directions, when passing through a soft soil layer, like the martian regolith. This amplification is caused by S-wave resonances in the soil column and is proportional to the impedance contrast between the soft surface layer and the more competent rock below (Takashi and Hirano 1941; Sánchez-Sesma and Crouse 2015). On Earth, this effect has been studied extensively as it can strongly increase earthquake damage (Borchardt 1970; Anderson et al. 1986). Similar site effects have also been observed in the Apollo lunar seismic data and correlated with the thickness of the regolith layer at the individual stations (Lammlein et al. 1974; Nakamura et al. 1975).

A popular method to assess the fundamental resonance frequency of a site is the H/V (horizontal to vertical Fourier spectral amplitude) ratio which can be quickly obtained from ambient vibration measurements (Nakamura 1989). The H/V curves obtained on soft soils generally show a clear peak at a frequency that correlates with the fundamental resonance frequency of the site (e.g. Lachet and Bard 1994; Lermo and Chávez-García 1994; Malischewsky and Scherbaum 2004). The physical interpretation of the H/V curve is still under discussion (Bonney-Claudet et al. 2006). Nakamura (2000, 2008) argues that SH wave resonances in low-velocity surface layer lead to the observed H/V peak. However, other authors point to the frequency-dependent Rayleigh wave ellipticity as explanation, where the frequency of the minimum in vertical Rayleigh wave energy depends on velocity and thickness of low-velocity surface layer (e.g. Lachet and Bard 1994; Lermo and Chávez-García 1994; Fäh et al. 2001; Bonney-Claudet et al. 2006). Bonney-Claudet et al. (2008) show for synthetic cases for a number of structural models that the H/V peak frequency provides a good estimate of the theoretical fundamental soil resonance, regardless of the contribution of different wave types to the wavefield. As these simulations also indicate that surface waves dominate the ambient vibration wavefield for moderate to high impedance contrasts between sediments and bedrock and surficial sources, we base the following analysis on the interpretation of site resonances in terms of Rayleigh wave ellipticity.

While the H/V peak frequency is thus independent of the actual wavefield composition, the peak amplitude, as confirmed by observations (e.g. Panou et al. 2005; Endrún et al. 2010; Endrún 2011), is not. Recent terrestrial studies using ambient vibrations either aim at extracting Rayleigh waves, in which case the H/V curve provides a measure of Rayleigh wave ellipticity (Hobiger et al. 2012), or at modeling of the complete noise wavefield using diffuse field theory (e.g. Sánchez-Sesma et al. 2011; García-Jerez et al. 2013; Kawase et al. 2015; Lontsi et al. 2015). Possible sources for ambient seismic noise on Mars include the atmosphere, i.e. winds, and thermal stresses. Winds had a strong influence on the Viking data recorded by a seismometer on top of the lander (Nakamura and Anderson 1979), and have been observed to generate Rayleigh waves propagating through the ground in terrestrial seismic data (Quiros et al. 2016). Diurnal variations in thermal stresses have been identified as the cause of frequent, weak, high-frequency events in the proximity of the Apollo stations on the Moon related to soil slumping (Duennenbier and Sutton 1974) which were used to extract Rayleigh wave group velocities via noise cross-correlation in the Apollo 17 Lunar Seismic Profiling Experiment (Larose et al. 2005). Tanimoto et al. (2008) related diurnal temporal variations of these group velocities to cyclic solar heating and thermal effects on the regolith's elastic parameters. As these proposed sources interact with the surface of the planet, they will predominantly generate surface waves and single station methods can be used to extract the Rayleigh wave ellipticity from these data. These methods are either

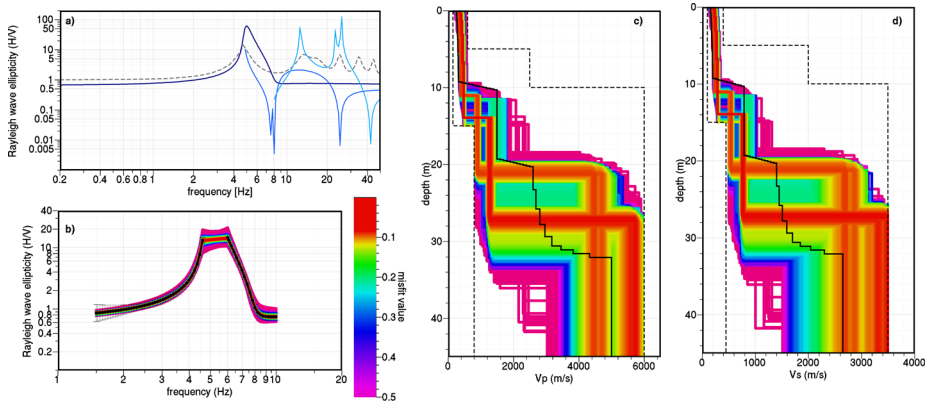


**Fig. 10** (a) Forward calculated ellipticity curves (blue curves) and SH response function (dashed black curve) for a reasonable velocity model based on orbital measurements and crater ejecta analysis. From dark to light blue, the ellipticity functions for the first three Rayleigh wave modes are shown. (b) Fit to the inverted data (left and right flank of the ellipticity peak, shown as black curves with error bars) for an inversion with a simple three-layer parameterization. (c)  $P$ -wave velocity models resulting from the inversion. Black curve is the input model for the forward calculations, and dashed lines mark the boundaries of the parameter space in the inversion. (d) Same as (c) for  $S$ -wave velocities

based on time-frequency analysis using a continuous wavelet transform (Fäh et al. 2001, 2009; Poggi et al. 2012), or on the random decrement technique (Hobiger et al. 2009, 2013; Bard et al. 2010). The measured ellipticity curves can then be inverted for shallow ground structure at the landing site. Scherbaum et al. (2003) have shown that inversions of Rayleigh wave ellipticity alone are subject to strong trade-offs between layer velocity and thickness. Accordingly, borehole information (e.g. Arai and Tokimatsu 2008) or surface wave dispersion (e.g. Dal Moro 2015) are often used as additional constraints. For InSight, information on wave velocities or regolith thickness derived from the analysis of the HP<sup>3</sup> hammering signal or from dust-devil generated Rayleigh waves could be used to *a priori* constrain the ellipticity inversion.

Here, we show an example for the inversion of a theoretical Rayleigh wave ellipticity curve calculated for a reasonable model of the shallow subsurface at the InSight landing site. Mapping of rocky ejecta craters in high-resolution orbital images and fragmentation theory based in impact crater measurements indicate a broken up regolith that is 2.4–17 m thick that is dominated by cohesionless sand or very low cohesion soils that grades into coarse, blocky ejecta that overlies strong, jointed bedrock (Pivarunas et al. 2015; Warner et al. 2016; Golombek et al. 2016, this issue). Regolith  $P$ - and  $S$ -wave velocities are derived from laboratory measurements on two volcanic sands (Delage et al. 2016, this issue).  $P$ -velocities for blocky ejecta, fractured and intact basalt are obtained from terrestrial field measurements on similar material (Wells et al. 1985; Vinciguerra et al. 2005).

The ellipticity curve is calculated for a model with 10 m regolith thickness (Fig. 10a), and typical error margins from terrestrial applications are assumed. A more detailed analysis and full wavefield modeling to demonstrate the extraction of Rayleigh waves from ambient vibration measurements is presented elsewhere (Knapmeyer-Endrun et al. 2016, this issue). The H/V peak observed in the forward calculation (Fig. 10a) is clearly related to the thickness of the regolith layer and the associated velocity contrast by the  $\lambda/4$  rule of thumb (e.g. Malischewsky and Scherbaum 2004). With a peak frequency of 5 Hz, it lies well within the frequency range covered by both the broadband and the short period seismometers. While

teleseismic recordings will not be affected by site amplification around this frequency, it would increase the horizontal components' amplitudes in the study of closer events. The ellipticity peak, as well as the details of the ratio on its right and left flanks are inverted with the Conditional Neighbourhood Algorithm (Sambridge 1999; Wathelet 2008) as implemented in GEOPSY (Wathelet et al. 2004, [www.geopsy.org](http://www.geopsy.org)). Like the Bayesian methods discussed in Sect. 3, the method relies on random sampling of the model space, which allows us to investigate uncertainty and non-uniqueness in the inversion. The inverse model was parameterized as consisting of three layers: regolith with low velocities increasing according to a power law to a depth of 5–15 m, an intermediate layer 5–30 m thick to represent the coarse ejecta/fractured basalt, and basaltic basement with  $P$ - and  $S$ -wave velocities above 3000 m/s and 1500 m/s, respectively. Results from five inversion runs starting with different random seeds are shown (Fig. 10). All models with a misfit value below 0.26 can explain the ellipticity curve within the given error bars (Fig. 10b). Though the model parameterization of the inversion is considerably simpler than the actual input model which contains gradational variations between layers and two separate layers for the coarse ejecta and the fractured basalt on top of the intact material, the inversion results recover the main parameters of the model well (Figs. 10c and d). While the regolith velocities are slightly overestimated, the regolith thickness estimates cluster around 10.8 m and 13.7 m, compared to an actual thickness of 10 m, in two distinct families of models. The difference between the two families is characterized by the mentioned depth-velocity trade-off occurring in the deeper layers. The first family, with the shallower regolith thickness, also provides reasonable estimates for the depth to the contact between coarse ejecta and fractured basalt and the velocity of the basement, although these parameters are in general less well constrained than those in the shallow layers. A tighter constraint on the maximum regolith thickness, e.g. from analysis of the seismic recordings of HP<sup>3</sup> signals or mapping of rocky crater ejecta, would help to distinguish between the model families, and in turn results in tighter constraints on the deeper structure from the ellipticity inversion.

## 5 Crustal Modeling with Receiver Functions and Surface Wave Ellipticity

Receiver function modeling of  $P$ -to- $S$  (Langston 1979) and, more recently,  $S$ -to- $P$  (Farra and Vinnik 2000) conversions has been a workhorse of passive seismic imaging of Earth's crust, mantle lithosphere, and transition zone structure. Receiver function modeling was also used on the Moon with seismic records originating from deep Moonquakes (Vinnik et al. 2001). In both cases, the location of the seismic source is not required when 3 axis seismic records are available. With teleseismic P and S waves of multiple marsquakes expected to be observed by InSight, receiver function modeling will yield new constraints on the internal crustal and lithospheric layering of Mars.

In this method, a free-surface transform can be used to estimate the incoming teleseismic and locally converted wavefields (Kennett 1991) from three component data, and the incoming wavefield is deconvolved from the scattered wavefield to remove source-side complexity and yield a receiver function. The lag time and amplitude of converted waves carries information on the depth and strength of the impedance contrast that produced them; variation with back-azimuth can be used to infer dipping layers and seismic anisotropy (e.g. Kosarev et al. 1984), although these are second order constraints compared to the depth and strength of the impedance contrast, which do not depend strongly on the source distance or location. Note that the strength of the impedance contrast can be a critical additional datapoint against

the non-uniqueness of solutions obtained with only differential travel times, as has been illustrated for the Moon (Lognonné et al. 2003). Because the presence of noise can destabilize deconvolution, a variety of deconvolution algorithms have been developed (e.g. Ligorría and Ammon 1999; Park and Levin 2000), including ones that fully quantify non-uniqueness and uncertainty associated with the deconvolution step (e.g. Kolb and Lekić 2014), or even dispense with the need for deconvolution by probabilistically accounting for source side effects (Dettmer et al. 2015).

Relating receiver functions to structure is a notoriously non-unique problem, since they are dominantly sensitive to changes in impedance across interfaces, rather than to absolute seismic velocities (Ammon et al. 1990). Therefore, model space search approaches, especially those that do not make assumptions on the number or location of structural layers beneath the receiver, show great promise. An additional source of uncertainty in receiver function interpretation from InSight stems from uncertainty in estimates of the ray parameter of the incoming teleseismic wavefield.

When the receiver functions are combined with complementary measurements, such as those of Rayleigh wave dispersion (Julia et al. 2000; Bodin et al. 2012) or ellipticity, receiver functions can dramatically reduce non-uniqueness of structural inferences, and yield reliable estimates of both absolute shear and compressional wave speeds. For the ellipticity measurements, we focus on a frequency band extending to lower frequencies than that used in Sect. 4.2, and focus on measurements from Rayleigh wave recordings from marsquakes rather than the ambient wave field. While ellipticity measurements are sensitive to shallower structure than surface wave dispersion measurements at the same frequency, they have been shown to be sensitive to crustal scale velocity structure on Earth (e.g. Tanimoto and Rivera 2008). Following the convention of Tanimoto and Rivera (2008), we take the ratio of the vertical component amplitude to the horizontal in this modeling, which is commonly termed the ZH ratio.

To simultaneously tackle these challenges of robust receiver function interpretation at Mars, we once again adopt a Bayesian approach to inversion. In this case, we use a transdimensional, hierarchical Bayesian joint inversion of receiver functions and Rayleigh wave ellipticity, which are both single-station measurements feasible with InSight. As in Sect. 3.4.2, allowing the number of model parameters to vary in a transdimensional approach makes no prior assumptions on the number or depth of structural layers, while being inherently parsimonious and yielding an ensemble of models that can be analyzed to fully quantify uncertainty and trade-offs.

In Fig. 11, we show the results of such an inversion for a synthetic model (dashed black line) where we have assigned a 10 % uncertainty for ZH ratio data and receiver function uncertainties 10 times larger than those obtained at a temporary broad band seismometer deployed on Earth (station M12A of the Transportable Array). The synthetic model is the same model for Mars as used in Sects. 3.2 and 3.3. We include 9 different receiver function inputs calculated for ray parameters ranging from 0.06–0.1 s/km, which corresponds to a distance range of 40°–90° in model A from Sohl and Spohn (1997) or 70°–90° in the synthetic model used in this section. To include information from crust and mantle lithosphere reverberations (i.e. multiples), which allow better constraints to be placed on  $V_P$  and  $V_S$ , we use receiver functions with a maximum lag time of 100 seconds following the P arrival. Separate, flexible parameterization is used for density and seismic velocity, because the expected resolution of density is low and is not shown in Fig. 11. No anisotropy or dipping layers are included in this test. The inclusion of multiples in the modeling procedure also increases the non-linearity of the inverse problem. We apply a “simulated annealing” type technique (Kirkpatrick et al. 1983) to improve the convergence of the McMC algorithm

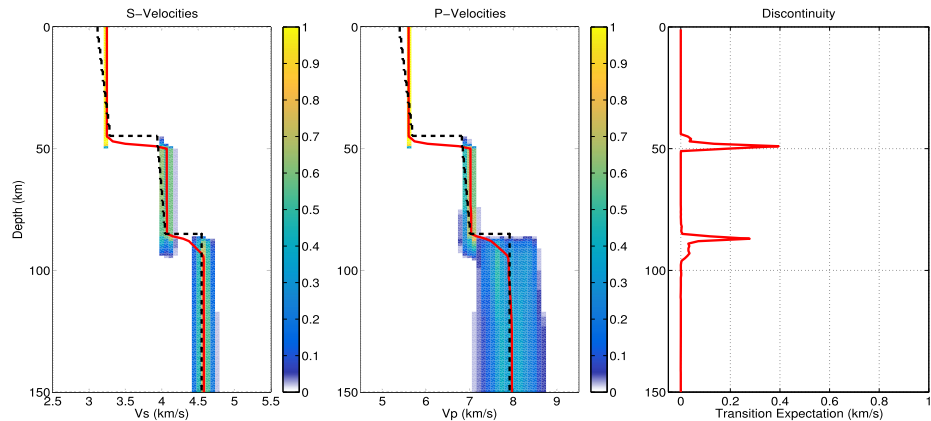


**Fig. 11** Probability density functions (PDFs) for  $V_S$  (left) and  $V_P$  (middle) obtained from a Bayesian inversion of synthetic receiver functions combined with surface wave ellipticity measurements. The right panel shows discontinuity transition expectation, which is the product of the probability of a jump at a given depth with the average shear velocity change of the jump. The input model is shown by the black dashed line, and the mean model from each PDF is shown with a red line

used here. We start by fitting low-pass filtered versions of the receiver functions (central frequency of 0.1 Hz) together with the ZH ratio data. After every  $10^5$  iterations, we include higher frequencies in the receiver functions (central frequencies of 0.2 Hz and 0.33 Hz) and continue the McMC with the current model. At lower frequencies, receiver functions tend to have simpler waveforms and are easier to fit, thereby reducing the chance of the McMC getting trapped at local minima. By slowly increasing the range of frequencies included in the analysis, we allow more detailed structure to be inferred from the data, while still keeping the sampling close to the global minimum. Figure 11 shows the profiles of  $V_P$  and  $V_S$  obtained after including the 0.33 Hz center frequency receiver function together with ZH ratio data. We can see that we are able to not only recover the profile of  $V_S$  in the crust and mantle lithosphere, but also that of  $V_P$ , as well as the depths of major discontinuities (Fig. 11).

If we have receiver functions recorded from several different epicentral distances (and, therefore, varying incoming ray parameters), it is possible to use receiver function data on its own to resolve major discontinuities. However, supplementing receiver functions with ZH ratio data greatly improves our ability to constrain the velocity structure. Indeed, as can be seen in the transition expectation value, which peaks at two distinct depths in Fig. 11, the mid-crustal discontinuity and crust-mantle boundary are clearly resolved. Constraining the crustal thickness beneath the landing site allows us to place much tighter constraints on our estimates of global crustal structure. Global scale modeling of gravity and topography variations (e.g. Neumann et al. 2004) give good constraints of the variation of crustal thickness of Mars, but do not constrain the average crustal thickness. When gravity and topography data are modeled using the assumption of isostasy, the 1-sigma uncertainties in average crustal thickness are found to lie between 33 and 81 km (Wieczorek and Zuber 2004). Using seismic data from InSight to constrain the crustal thickness at the landing site, however, allows us to anchor those global models and greatly tighten our constraints on crustal thickness everywhere on Mars.

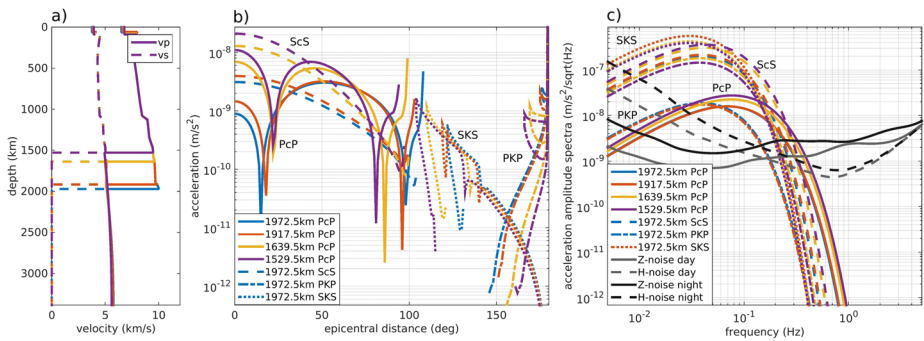


**Fig. 12** Ray theoretical spectral ground acceleration amplitude predictions for seismic phases reflected at the core-mantle boundary (PcP, ScS) or transmitted through the core of Mars (PKP, SKS) for a *surface* source with a seismic moment of  $10^{16}$  Nm ( $M_w$ 4.6). (a) Seismic velocity profiles for various core sizes based on the bulk composition model of Dreibus and Wänke (1985) (Fig. 1) for the amplitude, travel-time and ray parameter predictions in Figs. 12 and 13. (b) Amplitudes as predicted by ray theory with respect to epicentral distance at frequencies of 0.25 Hz. The minima in PcP amplitude at  $25^\circ$  to  $30^\circ$ , and  $85^\circ$  to  $105^\circ$  epicentral distance correspond to a phase shift in the complex reflection coefficient for reflections at the core mantle boundary. (c) Ground acceleration amplitude spectra of PcP, PKP, horizontally polarized ScS and vertically polarized SKS signals for the models in (a) at  $60^\circ$  epicentral distance for core-reflected phases PcP and ScS, and at  $170^\circ$  epicentral distances for core-transmitted phases PKP and SKS. Black and grey lines mark the mean InSight lander noise (Mimoun et al. 2016, this issue)

## 6 Observation of Core and Deep Mantle Phases

The seismic sampling of the deep interior of Mars is possible if the amplitudes of seismic phases reflected off or transmitted across the core-mantle boundary (CMB) fall above the predicted mean martian background noise of  $10^{-9} \text{ m}/(\text{s}^2 \text{Hz}^{1/2})$  (Murdoch et al. 2015; Mimoun et al. 2016, see Fig. 12). The ray theoretically predicted amplitudes for a medium seismicity support a likely observation of P and S energy interacting with the Martian CMB for events with greater than  $M_w$ 4.5 ( $\sim 10^{16}$  Nm). For the mission duration, we would expect to record on the order of 10 events of at least this magnitude (Fig. 3).

Figure 12b and c show spectral ground acceleration amplitudes of core reflected and transmitted phases on Mars for models based on the bulk composition of Dreibus and Wänke (1985) (Figs. 1 and 12a) while assuming different core radii consistent with recent moment of inertia and  $k_2$  Love number measurement (Konopliv et al. 2016; Genova et al. 2016). Amplitudes are calculated considering attenuation as well as geometric spreading and reflection/transmission coefficients at discontinuities encountered along the ray path (Aki and Richards 2002). Core-reflected amplitudes vary over almost one order of magnitude for events very close to the receiver, and for events at  $40^\circ$  epicentral distance. Amplitudes for core-transmitted phases show strong variation for events close to the antipode (Fig. 12b). For events with magnitudes above  $10^{16}$  Nm, PcP, ScS, PKP as well as SKS signals are expected to lie above the lander noise (Fig. 12c). Thus, seismic energy interacting with the Martian core-mantle boundary may be observable even in unfiltered and unstacked data, contrary to seismic data recorded by the Apollo missions sampling the deep interior of the Moon (e.g. Nakamura 2005; Lognonné and Johnson 2007; Knapmeyer 2009).

Predicted travel-time curves for core phases on Mars are shown in Fig. 13a for an event at the surface. Single station techniques already outlined for the InSight mission (Panning et al. 2015; Khan et al. 2016; Böse et al. 2016) may determine epicentral distance within an error of approximately 5 % for large enough events, facilitating the determination of abso-

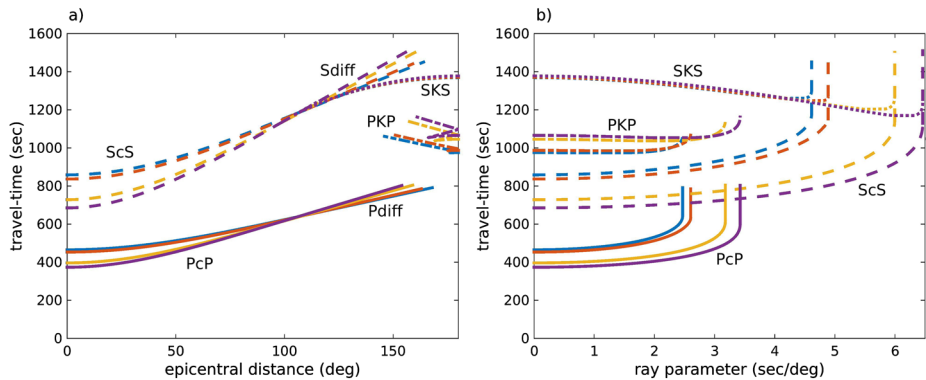


**Fig. 13** Travel-time as a function of epicentral distance and ray parameter for PcP and Pdiff, PKP, ScS and Sdiff signals as well as SKS for a surface source. Travel-times are computed for bulk compositions as in Fig. 12 with various core sizes as shown in Fig. 12(a). (a) Absolute travel-times as a function of epicentral distance. (b) Travel-times as a function of ray parameter, which can be determined through polarization analysis of a phase arrival at a three-component station. Maximum ray parameters for PcP/PKP/Pdiff and ScS/SKS/Sdiff are a function of the core size

lute travel-times (Figs. 13a and b). With decreasing core size, core-reflected and -transmitted waves arrive at steeper angles, and thus lower ray parameters (Fig. 13b). Thus, the determination of absolute travel-times as a function of ray parameter for epicentral distance ranges of 100 to 150° allows us to estimate the transfer from PcP/PKP to Pdiff and ScS/SKS to Sdiff, and therefore an estimation of the P and S core shadow (see Knapmeyer 2011).

The resolution of core phases on Mars can be further improved by applying stacking techniques to account for the expected background noise and interfering seismic phases, especially due to triplications possibly caused by an analog to the Earth's mantle transition zone at depths between approximately 1000 to 1500 km. These stacking techniques are commonly applied on Earth to improve detection of seismic energy of low signal-to-noise ratio (Schweitzer et al. 2002; Deuss 2009; Rost and Thomas 2009; Schmerr et al. 2013) and were also used to infer the radial structure of the lunar core as well as that of an overlying partial melt layer (Weber et al. 2011; Garcia et al. 2011; Khan et al. 2014). Even if source depth and source location for any given event may have large uncertainties during a single-station mission to Mars, different phases can be distinguished by their slownesses. In principle, slowness can be directly estimated from a single arrival based on polarization, although such an estimate may have significant errors. With multiple events, however, we can improve our estimation of slowness by examining coherence of arrivals in distance and time across multiple events, although the error of this estimation will require careful error propagation from the uncertain distance determinations. Prior to the summation of the traces of individual events, signals are aligned to a reference phase, e.g. the PcP onset assuming various core radii as applied to deep moonquakes. A maximum in signal coherency corresponds to the best fitting core radius. In the case of lunar seismograms, the coherency of the stacked signals can even be further improved by applying polarization filters (Jarosch 1977; Weber et al. 2011). Such filtering may also be useful on Mars depending on the scattering environment of the shallow martian regolith.

Core detection using seismic data with a single-station mission to Mars has a high potential for success, since ray-theoretical modeling through preliminary martian structure models such as the model by Rivoldini et al. (2011) predict amplitudes above the expected lander noise (Fig. 12). Determining relative PcP-P and ScS-P travel-times in the pre- or post-stacks

(Fig. 13) as a function of ray parameter allows for a core size estimate independent of source location, and the identification of the onset of Pdiff and Sdiff phases. Diffracted phases indicate the size of the core shadow and can be used to give an additional constraint on the core size (Oldham 1906; Knapmeyer 2011). This method, however, requires strong seismicity at an epicentral distance range between 100° and 150° due to the difficulty of determining a reasonably precise onset of Pdiff or Sdiff phases using data detected at a single station.

A valuable additional target for constraining the temperature and pressure state of the mantle would be sharp mantle transition zone discontinuities analogous to those on Earth interpreted as indicators of the phase transitions from olivine to wadsleyite and ringwoodite (e.g. Lay and Wallace 1995; Deuss 2009). However, due to different physical conditions (lower pressure and temperature) and the expected higher iron content of the martian mantle compared to the Earth's mantle, thermodynamic models constructing the phase equilibria (Khan and Connolly 2008; Rivoldini et al. 2011) show more gradual phase transitions in the orthopyroxene (~800 km) and the olivine-wadsleyite-ringwoodite-perovskite system (~1100 km and ~1400 km, respectively). Hence, contrary to Earth models like PREM, ray theory does not predict seismic reflections for the velocity models in Fig. 1. Some earlier models using slightly different composition and assumed thermal profiles (e.g. Okal and Anderson 1978; Sohl and Spohn 1997) show sharper transitions which can produce reflections. However, even for these models, the expected amplitude of the reflections as predicted by ray theory are significantly weaker than the core reflected phases, and so seismic phases interacting with these discontinuities are likely to be quite difficult to observe.

## 7 Normal Modes and Tides

Normal modes, or free oscillations, are the finite frequency response of a planet, and their frequencies do not depend on the excitation processes. Normal modes were therefore an early proposal as the ideal way to obtain the internal structure of Mars with a single station (e.g. Bolt and Derr 1969), and discussed again by papers published during the design phase of Viking and Mars96 respectively (Okal and Anderson 1978; Lognonné and Mosser 1993). The instruments finally delivered for these two missions nevertheless lacked sufficient long period response to observe normal modes. Instruments developed since the early 90's, however, provide the necessary long period sensitivity, even if limited by thermal noise at very long period (Lognonné et al. 1996, 2000).

The excitation of normal modes by marsquakes was studied by Lognonné et al. (1996) and later by Gudkova and Zharkov (2004). Both studies concluded that the observation of normal modes between 5 and 20 mHz with a noise level of  $10^{-9}$  m/(s<sup>2</sup> Hz<sup>1/2</sup>) will be possible from stacked records of multiple smaller quakes with a cumulative  $10^{18}$  Nm moment or from single-record analysis of the greatest quakes. This level of seismicity would be towards the upper end of reasonable expectations during the nominal mission (Fig. 3), and so such observations may be possible during the InSight mission, although certainly not guaranteed. The required noise performance, though, is consistent with the expectations for the InSight VBBs during night operation. The amplitude of the continuously excited normal modes are less constrained. Kobayashi and Nishida (1998) estimated Mars' hum level to be comparable to the Earth's in amplitude of the order of 3 nanogals. Amplitudes in the range of  $0.5\text{--}1 \times 10^{-9}$  m/(s<sup>2</sup> Hz<sup>1/2</sup>) are therefore expected, as on Earth. Smaller amplitudes were modeled by Lognonné and Johnson (2007), but at periods longer than 300 s. Recent simulations by Nishikawa et al. (2016) confirm amplitudes near  $10^{-9}$  m/(s<sup>2</sup> Hz<sup>1/2</sup>) at 100 s.

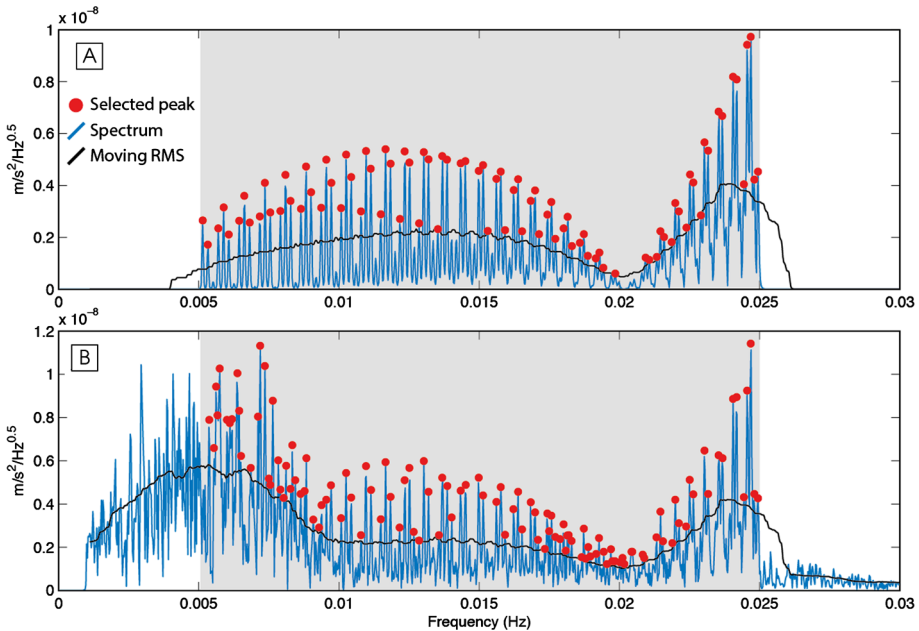


**Fig. 14** Noise-free (**a**) and noisy (**b**) spectra used to compute the eigenfrequencies used in the inversions. Only the peaks with an amplitude larger than a moving RMS (black line) are considered. These are shown in red

The detection of normal modes is therefore likely during night measurements when the external wind/pressure and temperature noise are at a minimum. We therefore illustrate in this section the inversion capability of these normal modes frequencies. Normal modes have been used extensively for inversion of the Earth structure, including very early usage of Monte-Carlo techniques (e.g. Press 1968), and have led to increasingly accurate Earth models, including PREM, one of the most widely used Earth reference models (Dziewonski and Anderson 1981).

We illustrate here a simple inversion of fundamental mode eigenfrequency. The eigenfrequency values are estimated from the maximum of the peaks detected in the synthetic signals presented in Sect. 3 (Fig. 5). The periods of the data modeled range between 40 and 200 s (0.005 to 0.025 Hz). We consider all the frequency peaks with an amplitude higher than a moving window root mean squared (RMS) average, with window length arbitrarily set to define 61 evenly spaced intervals over the entire time series. The uncertainty on each eigenfrequency value is set to be 1/4 of the width at half the peak's amplitude. These uncertainties are dependent on the signal's length. The spacing of Mars fundamental spheroidal normal modes is about 0.2 mHz. With an 8 hour time series, a frequency resolution of 0.035 mHz is achieved, corresponding to about 1/7 of the spacing between two modes. The optimum length of record will depend on both the seismic noise and the attenuation of normal modes. The attenuation is expected to be consistent with a quality factor in the range of 100–150, based on extrapolation of the Phobos tidal attenuation (e.g. Lognonné and Mosser 1993).

Figure 14 shows the spectra of the noise-free signal and of the same signal with expected instrumental and environmental noises added (same noise model as discussed in Sect. 3). Selected peaks for the inversions are also indicated. We use a similar inversion process as the one described in Sect. 3. The MINEOS package is used to compute the eigenfrequencies

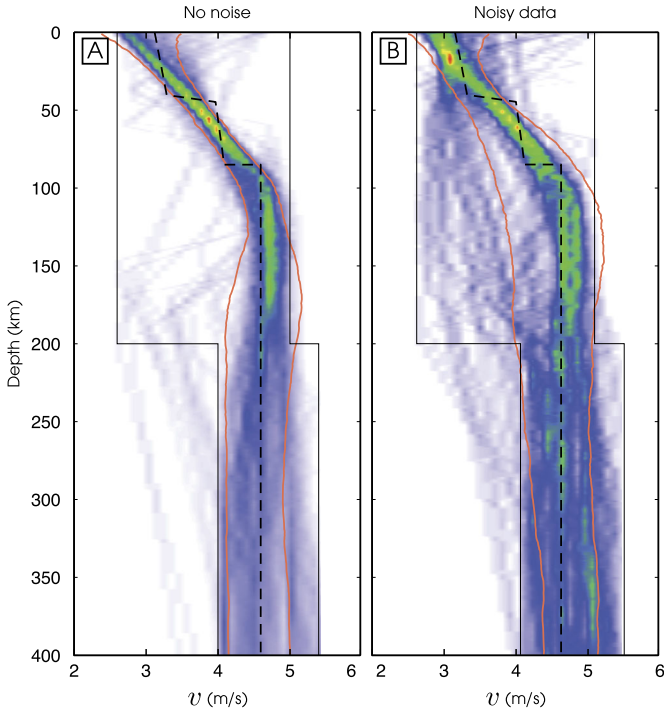


**Fig. 15** Results of the normal mode inversion. The black dashed lines show the model to retrieve. (a) and (b) show *a posteriori* probability density functions (PDF) of S wave velocity. Red and blue colors show high and low probabilities, respectively. Continuous black lines represent the minimum and maximum parameter values allowed. Orange curves delimit the interval between  $\pm 1\sigma$  of the median profile of the distribution. (a) and (b) are the results from the inversion of eigenfrequencies with no noise and including noise, respectively

of the investigated velocity models. We favor and converge towards models that produce a larger number of corresponding eigenfrequencies (within the uncertainties ascribed). The results for inversions with noise-free and noisy data are shown in Figs. 15a and 15b, respectively. In both cases, the input model (in dashed lines) is retrieved down to  $\sim 200$  km depth. The  $V_S$  model distribution is not as well defined for the noisy data, due to the presence of frequencies, not related to the event, introduced by the noise. Further work will be done to improve the detection of eigenfrequencies within the spectrum and the misfit function, but with these two examples we show the potential of using normal modes to explore the martian crust and upper mantle.

Several future improvements are expected, such as those leading to an identification of the angular orders of the peaks (not used in this example) or those improving the quality of the mode's signal to noise ratio with multiple taper methods (e.g. Park et al. 1987). Neither the seismic moment of the largest expected quake nor the strength of the hum excitations will be large enough, however, to excite in a detectable way the lowest angular order normal modes which are sensitive to the deep structure of the planet, including the core. The inversion of the Love number, through the gravimetric factor—a function of the  $h$  and  $k$  Love numbers that is defined as the ratio between tidal gravity variations of the planet compared with those expected for a rigid body (e.g. Dehant and Ducarme 1987)—will therefore put important additional constraints on the core size, in addition to those provided by SEIS for the core phases described in Sect. 6 and by RISE (which will determine very precise or-

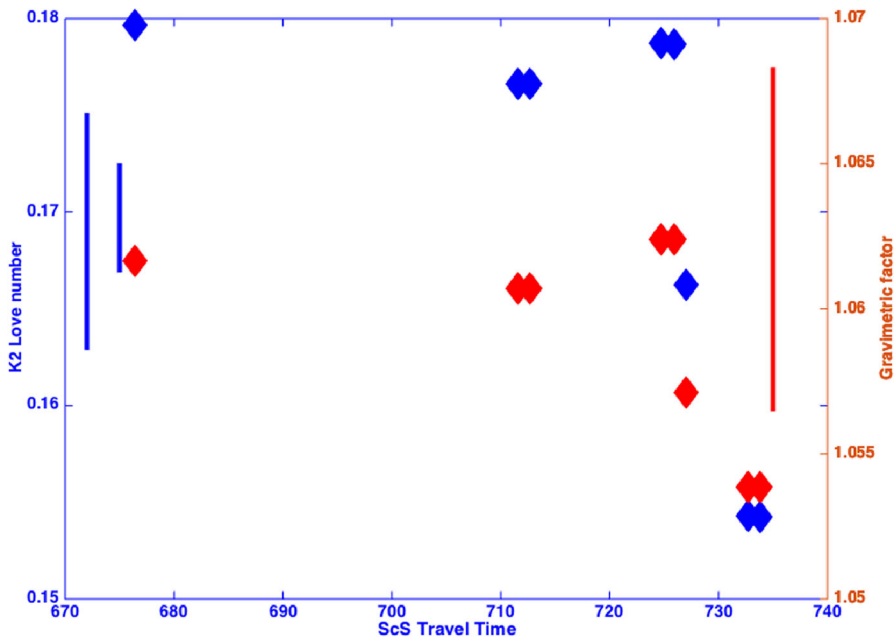


**Fig. 16** Models are arranged by increasing ScS travel times and are from left to right: EH45Cold without crust, DWThotCrust1, DWThotCrust1r, EH45ThotCrust2, EH45ThotCrust2r, DWThot, EH45TcoldCrust1 and EH45TcoldCrust1r. Models with r have a thin layer of 1 km bedrock below an 80 m regolith. Crust1 and Crust2 have different crustal structure. DW mantle bulk composition is from Taylor (2013), while EH45 mantle bulk composition is from Sanloup et al. (1999). Hot and cold temperature profiles are from Plesa et al. (2016) (Fig. 2). The resolution of ScS picking will mainly depend on the attenuation of these waves and will likely be much better than 5 s. If detected, ScS will therefore be a much stronger constraint, but the gravimetric factors and Love number will nevertheless be able to separate models with similar ScS, as shown for the EH45ThotCrust2, DWThot and EH45TcoldCrust1 on the right side of the figure. The *left blue bar* is the range for the  $k_2$  measurement from Konopliv et al. (2016), while the *right red bar* is the error bar for an  $\pm 0.5\%$  error in the tide measurement

bital parameters through radio tracking of the lander), through the measurement of Mars' nutation. These can be combined with the Love number  $k_2$ , already measured from precise tracking data (e.g. Konopliv et al. 2016; Genova et al. 2016). We illustrate the complementarity of these constraints with Fig. 16, where both the ScS travel times (at 1 Hz), the gravimetric factors (at Phobos tidal period) and the  $k_2$  Love numbers (at solar tidal period) are shown for the models DW and EH45, either hot or cold. A power law dependence for Q, comparable to Earth physical dispersion models (e.g. Lekić et al. 2009) and used for Mars by Lognonné and Mosser (1993) and Zharkov and Gudkova (1997), has been used with alpha  $\sim 0.05$ , which predicts Q factors of 86 and 90 for Solar and Phobos tide and shear Q in the mantle of 143 at 1 Hz. The alpha value was chosen in this case so the Phobos Q is in the range of observations (e.g. Bills et al. 2005). This relationship predicts physical dispersion that decreases the shear modulus by about 3 % between 1 Hz and solar tide, while an increase of about 0.5 % in the Love number is expected between Phobos and Solar tides. This model for attenuation is, however, not unique, and other dispersion models can be used, such as those proposed by Jackson and Faul (2010). For SEIS, the largest constraint will be related to the absolute calibration of the seismometer gravity output, which we require to be  $\pm 0.35\%$ , in order to contain the core size estimate to  $\pm 0.5\%$ . All these data will finally be

used for more complete inversion of the deep interior, which will be important in decreasing trade-offs between core size and possible low shear modulus structure in the lower mantle.

## 8 Discussion and Conclusions

The MSS plans on developing models covering a variety of depth ranges, from very near surface techniques to look at regolith thickness all the way to normal mode observations sensitive to averages of global structure from the surface to the core. In the process, we will also use a variety of seismic data types, as well as including results from heat flow measurements of HP<sup>3</sup> and core radius and state from the RISE radio science.

### 8.1 Strengths of Bayesian Modeling

While initial work may focus separately on using particular data types to look at particular aspects of the interior, one of the critical aims of our modeling effort is to use Bayesian approaches that allow us to accommodate different data types or models inferred from them in a very natural framework. This can be done in two different ways: joint inversions of multiple data types, and including modeling results from particular data types as prior constraints in Bayesian modeling.

It is quite natural to do joint inversions of multiple data types with Bayesian approaches. Relative data weighting, which is a persistent challenge in joint inversions with data types that may not have well defined data variance estimates, can even be accommodated with hierarchical approaches (e.g. Bodin et al. 2012) which treat data variance as an additional uncertain parameter, thus allowing us to quantify additional uncertainties arising from varying data weighting schemes. However, joint inversions may not always be practical. For example, normal mode constraints and HP<sup>3</sup> hammering signals operate on such different length scales that attempting to model both simultaneously is not useful. However, modeling results can be used to constrain the prior probabilities that govern Bayesian inversions. For example, crustal thickness constraints from receiver functions, and core radius constraints from RISE data can be used to define the *a priori* estimates that go into a Bayesian inversion of body wave and surface wave observations for mantle structure. As another example, HP<sup>3</sup> heat flow measurements can be used to define tighter prior constraints on the input thermal profile for the modeling including mineral physics constraints as in Sect. 3.4.1.

### 8.2 Lateral Variations

The seismic simulations and modeling discussed so far consider radially symmetric models. The effect of Mars topography and crustal thickness variations on long-period surface waves (periods longer than 80 s) were previously investigated by Larmat et al. (2008) where up to 6 s time shifts and within about 4 % amplitude variations were reported due to the crustal dichotomy between the northern and southern hemispheres. To better model what we may expect from the InSight mission, we performed higher-resolution numerical simulations to examine the effect of 3D variations on shorter-period global ( $>\sim 10$  s) and regional ( $>\sim 2$  s) seismic waves (Bozdağ et al. 2016). For global simulations, we use the open source spectral-element solver SPECFEM3D\_GLOBE, originally developed by Komatsch and Tromp (2002a,b), which accommodates 3D elastic and anelastic seismic models, as well as effects due to topography, gravity, rotation, and ellipticity. We first implemented a 1D Mars model constructed by Sohl and Spohn (1997) with a 110 km thick crust and a 1D *Q*-profile

adapted from the 1D Earth model PREM (Dziewonski and Anderson 1981). We then included the effects of ellipticity, gravity and rotation (Williams 2016). Using 3D crustal thickness variations determined from gravity measurements by Wieczorek and Zuber (2004) and high-resolution topography from the Mars Orbiter Laser Altimeter (MOLA), we investigated effects of surface topography and the dichotomy in crustal thickness between Mars' southern and northern hemispheres on seismic waves with periods down to  $\sim$ 10 s. To assess the stability and robustness of numerical simulations, we benchmarked SPECFEM3D\_GLOBE seismograms computed for the 1D reference model (Sohl and Spohn 1997) to those from the 2.5D axisymmetric spectral-element solver AxiSEM (Nissen-Meyer et al. 2014) down to 10 s. Furthermore, we demonstrated the 3D crustal effects, not only thickness variations but also 3D wavespeed variations within the crust, on regional waveforms using the regional spectral-element solver SES3D (Fichtner et al. 2009), which uses regular grids on spherical coordinates, down to 2 s. Our initial experiments show that the numerical tools are ready for examining various realistic wave propagation scenarios on Mars using different seismic models as well as sources.

As our amount of data increases, we may be able to start using events recorded from different source regions to constrain how much variation in crust and mantle structure we actually have on Mars. Determining the degree 2 structure of the planet will require at least 5 quakes with R1 and R3 measurements. Using these measurements, we can constrain great-circle average structure which depends mostly on the spherical harmonic degree 2 structure and has no sensitivity to odd degrees. Such a goal is likely within 1-2 martian years. The determination of the degree 1 and 3 of the planet will, however, be more challenging, as they will require the use of R1, R2 and R3 which can provide the origin time, location and group velocity. Relative comparison of the R1 and R2 dispersion of surface waves can nevertheless allow for determination of the differences in crustal and lithosphere structure between the north and south hemisphere.

### 8.3 Interaction with Marsquake Service

The two operational services of the SEIS instrument team (MSS and MQS) are necessarily closely related. Accurate structure models improve quake location, while accurate quake location is essential for better resolution of structure. Throughout the mission, engagement between these services will be essential. Some of the techniques described here are actually simultaneous inversions for structure and source parameters, and so do not fit easily into a silo concept where separate researchers work only on one side of the problem. Communication and crossover between the management and products of both of these groups will foster the best results in delivering the desired science outcomes from the InSight mission.

### 8.4 Planetary Data System Deliverables

The SEIS team has the responsibility to deliver several products to the final, official Planetary Data System (PDS) archive for the InSight mission. These include calibration and instrument transfer function information prior to landing and after calibration on the martian surface, and raw and calibrated continuous and event-specific data from both the broadband and short period instruments as well as engineering temperature on a quarterly basis. Finally, SEIS is responsible for delivering a set of geophysical structure and seismic velocity models (from MSS) and a seismic source catalog (from MQS) 5 months after the end of mission.

While the PDS archive is not required until after the end of the mission, both MSS and MQS will be making products available to the community with frequent updates whenever

new data becomes available. In particular, data will be archived in the IRIS (Incorporated Research Institutions for Seismology) Data Management Center (DMC) soon after it is verified for quality. This will allow the final archived version to represent a mature set of models and structure catalogs based on evolving data and improved methodologies through the course of the mission.

## 9 Conclusions

Based on estimates of seismic activity levels on Mars, we anticipate recovery of seismic data capable of resolving structure on a wide variety of length scales. Initial models will be based on body wave and surface wave data which does not rely strongly on *a priori* knowledge of structure, as well as approaches that allow for simultaneous inversion of structure and source parameters. Shallow site response can be analyzed with signals from the HP<sup>3</sup> hammering as well as high frequency measurements of surface wave ellipticity. Crustal scale structure can be resolved with receiver functions and lower frequency measurements of surface wave ellipticity. Ray theory modeling suggests that we should be able to observe core-interacting phases to better resolve properties of the martian core. Normal modes observations are feasible and can constrain globally averaged structure. Data from a single seismic station on Mars by the InSight lander will enable us to greatly improve our understanding of the interior structure of the planet.

**Acknowledgements** Research described in this paper was partially done by the InSight Project, Jet Propulsion Laboratory, California Institute of Technology, under a contract with the National Aeronautics and Space Administration. This work has been supported by CNES for all French institutions' co-authors. S.H., J.B.G. and the IPGP, ISAE and Univ. Nantes teams have been also supported by ANR (ANR-14-CE36-0012 "Seismology on Mars") and PL by Institut Universitaire de France. The Bayesian inversions of Sect. 3 were performed using HPC resources of CINES (Centre Informatique National de l'Enseignement Supérieur) under the allocation 2015047341 made by GENCI (Grand Equipement National de Calcul Intensif). A.K. was supported by grants from the Swiss National Science Foundation (SNF-ANR project 157133 "Seismology on Mars") and from the Swiss National Supercomputing Centre (CSCS) under project ID s628. N.T. and J.W. were supported by funding from the U.K. Space Agency. The open source spectral-element software packages SPECFEM3D GLOBE and AxiSEM are freely available via the Computational Infrastructure for Geodynamics (CIG; [geodynamics.org](http://geodynamics.org)). For SPECFEM3D GLOBE simulations computational resources were provided by the Princeton Institute for Computational Science & Engineering (PICSciE). This paper is InSight Contribution Number 22.

## References

- K. Aki, P.G. Richards, *Quantitative Seismology*, 2nd edn. (University Science Books, Sausalito, 2002)
- C.J. Ammon, G.E. Randall, G. Zandt, On the nonuniqueness of receiver function inversions. *J. Geophys. Res.* **95**(B10), 15303–15318 (1990)
- D. Anderson, W. Miller, G. Latham, Y. Nakamura, M. Toksöz, Seismology on Mars. *J. Geophys. Res.* **82**, 4524–4546 (1977)
- J. Anderson, P. Bodin, J. Brune, J. Prince, S. Singh, R. Quaas, M. Onate, Strong ground motion from the Michoacan, Mexico, earthquake. *Science* **233**, 1043–1049 (1986)
- H. Arai, K. Tokimatsu, Three-dimensional Vs profiling using microtremors in Kushiro, Japan. *Earthq. Eng. Struct. Dyn.* **37**, 845–859 (2008). doi:[10.1002/eqe.788](https://doi.org/10.1002/eqe.788)
- W. Banerdt, S. Smrekar, P. Lognonné, T. Spohn, S. Asmar, D. Banfield, L. Boschi, U. Christensen, V. Dehant, W. Folkner, D. Giardini, W. Goetze, M. Golombek, M. Grott, T. Hudson, C. Johnson, G. Kargl, N. Kobayashi, J. Maki, D. Mimoun, A. Mocquet, P. Morgan, M. Panning, W. Pike, J. Tromp, T. van Zoest, R. Weber, M. Wieczorek, R. Garcia, K. Hurst, InSight: a discovery mission to explore the interior of Mars, in *44th Lunar and Planetary Science Conference, Lunar and Planetary Inst.*, Houston, TX (2013). p Abstract #1915. <http://www.lpi.usra.edu/meetings/lpsc2013/pdf/1915.pdf>

- P.Y. Bard, H. Cadet, B. Endrun, M. Hobiger, F. Renalier, N. Theodulidis, M. Ohrnberger, D. Fäh, F. Sabetta, P. Teves-Costa, A.M. Duval, C. Cornou, B. Guilier, M. Wathélet, A. Savvaidis, A. Köhler, J. Burjanek, V. Poggi, G. Gassner-Stamm, H.B. Havenith, S. Hailemikael, J. Almeida, I. Rodrigues, I. Veludo, C. Lacaue, S. Thomassin, M. Kristekova, From non-invasive site characterization to site amplification: recent advances in the use of ambient vibration measurements, in *Earthquake Engineering in Europe*, ed. by M. Garevski, A. Ansai. Geotechnical, Geological, and Earthquake Engineering, vol. 17 (Springer Science + Business Media B.V., Dordrecht, 2010), pp. 105–123. Chap. 5
- V. Belleguic, P. Lognonné, M. Wieczorek, Constraints on the Martian lithosphere from gravity and topography data. *J. Geophys. Res.* **110**(E11), 005 (2005). doi:[10.1029/2005JE002437](https://doi.org/10.1029/2005JE002437)
- P. Bézier, Définition numérique des courbes et surfaces I. *Automatisme* **11**, 625–632 (1966)
- P. Bézier, Définition numérique des courbes et surfaces II. *Automatisme* **12**, 17–21 (1967)
- B.G. Bills, A. Neumann, D.E. Smith, M.T. Zuber, Improved estimate of tidal dissipation within Mars from MOLA observations of the shadow of Phobos. *J. Geophys. Res.* **110**(E07), 004 (2005). doi:[10.1029/2004JE002376](https://doi.org/10.1029/2004JE002376)
- T. Bodin, M. Cambridge, H. Tkalcic, P. Arroucau, K. Gallagher, N. Rawlinson, Transdimensional inversion of receiver functions and surface wave dispersion. *J. Geophys. Res.* **117**(B02), 301 (2012). doi:[10.1029/2011JB008560](https://doi.org/10.1029/2011JB008560)
- B.A. Bolt, J.S. Derr, Free bodily vibrations of the terrestrial planets *Vistas Astron.* **11**, 69–102 (1969)
- S. Bonnefoy-Claudet, C. Cornou, P.Y. Bard, F. Cotton, P. Moczo, J. Kristek, D. Fäh, H/V ratio: a tool for site effects evaluation. Results from 1-D noise simulations. *Geophys. J. Int.* **167**, 827–837 (2006). doi:[10.1111/j.1365-246X.2006.03154.x](https://doi.org/10.1111/j.1365-246X.2006.03154.x)
- S. Bonnefoy-Claudet, A. Köhler, C. Cornou, M. Wathélet, P.Y. Bard, Effects of Love waves on microtremor H/V ration. *Bull. Seismol. Soc. Am.* **98**, 288–300 (2008). doi:[10.1785/0120070063](https://doi.org/10.1785/0120070063)
- R. Borchard, Effects of local geology on ground motion near San Francisco Bay. *Bull. Seismol. Soc. Am.* **60**, 29–61 (1970)
- M. Böse, J.F. Clinton, S. Ceylan, F. Euchner, M. van Driel, A. Khan, D. Giardini, P. Lognonné, W.B. Banerdt, A probabilistic framework for single-station location of seismicity on Earth and Mars. *Phys. Earth Planet. Inter.* (2016). doi:[10.1016/j.pepi.2016.11.003](https://doi.org/10.1016/j.pepi.2016.11.003)
- E. Bozdağ, Y. Ruan, N. Metthez, A. Khan, K. Leng, M. van Driel, C. Larmat, D. Giardini, J. Tromp, P. Lognonné, W.B. Banerdt, Simulations of seismic wave propagation on Mars. *Space Sci. Rev.* (2016, this issue)
- D.M. Burr, J.A. Grier, A.S. McEwen, L.P. Keszthelyi, Repeated aqueous flooding from the Cerberus Fossae: evidence for very recently extant, deep groundwater on Mars. *Icarus* **159**, 53–73 (2002). doi:[10.1006/icar.2002.6921](https://doi.org/10.1006/icar.2002.6921)
- H. Chenet, P. Lognonné, M. Wieczorek, H. Mizutani, Lateral variations of lunar crustal thickness from the apollo seismic data set. *Earth Planet. Sci. Lett.* **243**, 1–14 (2006)
- J.A.D. Connolly, Computation of phase equilibria by linear programming: a tool for geodynamic modeling and its application to subduction zone decarbonation. *Earth Planet. Sci. Lett.* **236**, 524–541 (2005)
- J.A.D. Connolly, The geodynamic equation of state: what and how. *Geochem. Geophys. Geosyst.* **10**(Q10), 014 (2009). doi:[10.1029/2009GC002540](https://doi.org/10.1029/2009GC002540)
- G. Dal Moro, Joint analysis of Rayleigh-wave dispersion and HVSR of lunar seismic data from the Apollo 14 and 16 sites. *Icarus* **254**, 338–349 (2015). doi:[10.1016/j.icarus.2015.03.017](https://doi.org/10.1016/j.icarus.2015.03.017)
- G.H. Darwin, A numerical estimate of the rigidity of the Earth. *Nature* **27**, 22–23 (1882). doi:[10.1038/027022b0](https://doi.org/10.1038/027022b0)
- I.J. Daubar, A.S. McEwen, S. Byrne, M.R. Kennedy, B. Ivanov, The current martian cratering rate. *Icarus* **225**, 506–516 (2013)
- P.M. Davis, Meteoroid impacts as seismic sources on Mars. *Icarus* **105**, 469–478 (1993)
- V. Dehant, B. Ducarme, Comparison between the theoretical and observed tidal gravimetric factors. *Phys. Earth Planet. Inter.* **49**, 192–212 (1987)
- P. Delage, F. Karakostas, A. Dhemaid, M. Belmokhtar, D. De Laure, J.C. Dupla, Y.J. Cui, An investigation of the geotechnical properties of some Martian regolith simulants with respect to the surface properties of the InSight mission landing site. *Space Sci. Rev.* (2016, this issue)
- J. Dettmer, S.E. Dosso, T. Bodin, J. Stipčević, P.R. Cummins, Direct-seismogram inversion for receiver-side structure with uncertain source-time functions. *Geophys. J. Int.* **203**(2), 1373–1387 (2015)
- A. Deuss, Global observations of mantle discontinuities using SS and PP precursors. *Surv. Geophys.* **30**, 301–326 (2009)
- G. Dreibus, H. Wänke, Mars: a volatile rich planet. *Meteoritics* **20**, 367–382 (1985)
- M. Drilleau, E. Beucler, A. Mocquet, O. Verhoeven, G. Moëbs, G. Burgos, J.P. Montagner, P. Vacher, A Bayesian approach to infer radial models of temperature and anisotropy in the transition zone from surface wave dispersion curves. *Geophys. J. Int.* **195**, 1165–1183 (2013)
- F. Duennebier, G.H. Sutton, Thermal moonquakes. *J. Geophys. Res.* **79**, 4351–4363 (1974)

- A. Dziewonski, D. Anderson, Preliminary Reference Earth Model. *Phys. Earth Planet. Inter.* **25**, 297–356 (1981)
- L.T. Elkins-Tanton, E.M. Parmentier, P.C. Hess, Magma ocean fractional crystallization and cumulate overturn in terrestrial planets: implications for Mars. *Meteorit. Planet. Sci.* **38**(12), 1753–1771 (2003). doi: [10.1111/j.1945-5100.2003.tb00013.x](https://doi.org/10.1111/j.1945-5100.2003.tb00013.x)
- L.T. Elkins-Tanton, S.E. Zaranek, E.M. Parmentier, P.C. Hess, Early magnetic field and magmatic activity on Mars from magma ocean cumulate overturn. *Earth Planet. Sci. Lett.* **236**, 1–12 (2005)
- B. Endrùn, Love wave contribution to the ambient vibration H/V amplitude peak observed with array measurements. *J. Seismol.* **15**, 443–472 (2011). doi: [10.1007/s10950-010-9191-x](https://doi.org/10.1007/s10950-010-9191-x)
- B. Endrùn, M. Ohrnberger, A. Savvidis, On the repeatability and consistency of ambient vibration array measurements. *Bull. Earthq. Eng.* **8**, 535–570 (2010). doi: [10.1007/s10518-009-9159-9](https://doi.org/10.1007/s10518-009-9159-9)
- D. Fäh, F. Kind, D. Giardini, A theoretical investigation of average H/V ratios. *Geophys. J. Int.* **145**, 535–549 (2001)
- D. Fäh, M. Wathelet, M. Kristekova, H. Havenith, B. Endrùn, G. Stamm, V. Poggi, J. Burjanek, C. Cornou, Using ellipticity information for site characterisation. NERIES JRA4 “Geotechnical Site Characterisation”, task B2, final report, EC project number: 026130 (2009)
- V. Farra, L. Vinnik, Upper mantle stratification by P and S receiver functions. *Geophys. J. Int.* **141**, 699–712 (2000)
- A. Fichtner, B.L.N. Kennett, H. Igel, H.P. Bunge, Full seismic waveform tomography for upper-mantle structure in the Australasian region using adjoint methods. *Geophys. J. Int.* **179** (2009). doi: [10.1111/j.1365-246X.2009.04368.x](https://doi.org/10.1111/j.1365-246X.2009.04368.x)
- W.M. Folkner, S.W. Asmar, V. Dehant, R.W. Warwick, The rotation and interior structure experiment (RISE) for the InSight mission to Mars, in *43rd Lunar and Planetary Science Conference, Lunar and Planetary Inst.*, Houston, TX (2012). p Abstract #1721. <http://www.lpi.usra.edu/meetings/lpsc2012/pdf/1721.pdf>
- J. Gagnepain-Beyneix, P. Lognonné, H. Chenet, D. Lombardi, T. Spohn, A seismic model of the lunar mantle and constraints on temperature and mineralogy. *Phys. Earth Planet. Inter.* **159**, 140–166 (2006)
- R. Garcia, J. Gagnepain-Beyneix, S. Chevrot, P. Lognonné, Very preliminary reference Moon model. *Phys. Earth Planet. Inter.* **188**, 96–113 (2011)
- A. García-Jerez, F. Luzón, F.J. Sánchez-Sesma, E. Lunedei, D. Albarello, M.A. Santoyo, J. Almendros, Diffuse elastic wavefield within a simple crustal model. Some consequences for low and high frequencies. *J. Geophys. Res.* **118**, 5577–5595 (2013). doi: [10.1002/2013JB010107](https://doi.org/10.1002/2013JB010107)
- A. Genova, S. Goosens, F.G. Lemoine, E. Mazarico, G.A. Neumann, D.E. Smith, M.T. Zuber, Seasonal and static gravity field of Mars from MGS, Mars Odyssey and MRO radio science. *Icarus* **272**, 228–245 (2016). doi: [10.1016/j.icarus.2016.02.050](https://doi.org/10.1016/j.icarus.2016.02.050)
- F. Gilbert, A. Dziewoński, An application of normal mode theory to the retrieval of structural parameters and source mechanisms from seismic spectra. *Philos. Trans. R. Soc. Lond. A* **278**, 187–269 (1975)
- M. Golombek, A revision of Mars seismicity from surface faulting, in *33rd Lunar and Planetary Science Conference, Lunar and Planetary Inst.*, Houston, TX (2002). p Abstract #1244
- M. Golombek, W. Banerdt, K. Tanaka, D. Tralli, A prediction of Mars seismicity from surface faulting. *Science* **258**, 979–981 (1992)
- M.P. Golombek, Constraints on the largest marsquake, in *25th Lunar and Planetary Science Conference* (1994), pp. 441–442
- M.P. Golombek, D. Kipp, N. Warner, I.J. Daubar, R. Ferguson, R. Kirk, R. Beyer, A. Huertas, S. Piqueux, N. Putzig, B.A. Campbell, G. Morgan, C. Charalambous, W.T. Pike, K. Gwinner, F. Calef, J. Ashley, D. Kass, M. Mischna, C. Bloom, N. Wigton, C. Schwartz, H. Gengl, L. Redmond, J. Sweeney, E. Sklyanskiy, M. Lisano, J. Benardino, S. Smrekar, W.B. Banerdt, Selection of the InSight landing site. *Space Sci. Rev.* (2016, this issue)
- T. Gudkova, V. Zharkov, Mars: interior structure and excitation of free oscillations. *Phys. Earth Planet. Inter.* **142**, 1–22 (2004)
- T. Gudkova, P. Lognonné, K. Miljković, J. Gagnepain-Beyneix, Impact cutoff frequency—momentum scaling law inverted from Apollo seismic data. *Earth Planet. Sci. Lett.* **427**, 57–65 (2015). doi: [10.1016/j.epsl.2015.06.037](https://doi.org/10.1016/j.epsl.2015.06.037)
- T.C. Hanks, D.M. Boore, Moment-magnitude relations in theory and practice. *J. Geophys. Res.* **B89**, 6229–6235 (1984)
- W.K. Hartmann, Martian cratering 8: isochron refinement and the chronology of Mars. *Icarus* **174**, 294–320 (2005)
- W. Hastings, Monte Carlo sampling methods using Markov chains and their applications. *Biometrika* **57**, 97–109 (1970)
- R.B. Herrmann, Computer programs in seismology: an evolving tool for instruction and research. *Seismol. Res. Lett.* **84**, 1081–1088 (2013). doi: [10.1785/0220110096](https://doi.org/10.1785/0220110096)

- M. Hobiger, P.Y. Bard, C. Cornou, N. Le Bihan, Single station determination of Rayleigh wave ellipticity by using the random decrement technique (RayDec). *Geophys. Res. Lett.* **36**(L14), 303 (2009). doi:[10.1029/2009GL038863](https://doi.org/10.1029/2009GL038863)
- M. Hobiger, N. Le Bihan, C. Cornou, P.Y. Bard, Multicomponent signal processing for Rayleigh wave ellipticity estimation: application to seismic hazard assessment. *IEEE Signal Process. Mag.* **29**, 29–39 (2012). doi:[10.1109/MSP.2012.2184969](https://doi.org/10.1109/MSP.2012.2184969)
- M. Hobiger, C. Cornou, M. Watheler, G. Di Giulio, B. Knapmeyer-Endrun, F. Renalier, P.Y. Bard, A. Savvidis, S. Hailemikael, N. Le Bihan, M. Ohrnberger, N. Theodoulidis, Ground structure imaging by inversions of Rayleigh wave ellipticity: sensitivity analysis and application to European strong-motion sites. *Geophys. J. Int.* **192**, 207–229 (2013). doi:[10.1093/gji/ggs005](https://doi.org/10.1093/gji/ggs005)
- I. Jackson, U.H. Faul, Grainsize-sensitive viscoelastic relaxation in olivine: Towards a robust laboratory-based model for seismological application. *Phys. Earth Planet. Inter.* **183**, 151–163 (2010). doi:[10.1016/j.pepi.2010.09.005](https://doi.org/10.1016/j.pepi.2010.09.005)
- W.L. Jaeger, L.P. Keszthelyi, A.S. McEwen, C.M. Dundas, P.S. Russell, Athabasca Valles, Mars: a lava-draped channel system. *Science* **317**, 1709–1711 (2007). doi:[10.1126/science.1143315](https://doi.org/10.1126/science.1143315)
- H.S. Jarosch, The use of surface reflections in lunar seismograms. *Bull. Seismol. Soc. Am.* **67**(6), 1647–1659 (1977)
- J. Julia, C.J. Ammon, R.B. Herrmann, A.M. Correig, Joint inversion of receiver function and surface wave dispersion observations. *Geophys. J. Int.* **143**(1), 99–112 (2000)
- H. Kawase, S. Matsushima, T. Satoh, F.J. Sánchez-Sesma, Applicability of theoretical horizontal-to-vertical ratio of microtremors based on the diffuse field concept to previously observed data. *Bull. Seismol. Soc. Am.* **105** (2015). doi:[10.1785/0120150134](https://doi.org/10.1785/0120150134)
- S. Kedar, J. Andrade, W.B. Banerdt, P. Delage, M. Golombek, M. Grott, T. Hudson, A. Kiely, M. Knapmeyer, B. Knapmeyer-Endrun, C. Krause, T. Kawamura, P. Lognonné, W.T. Pike, Y. Ruan, N. Teanby, J. Tromp, J. Wookey, Analysis of regolith properties using seismic signals generated by InSight's HP<sup>3</sup> penetrator. *Space Sci. Rev.* (2016, this issue)
- B. Kenda, P. Lognonné, A. Spiga, T. Kawamura, S. Kedar, W.B. Banerdt, R.D. Lorenz, Modeling of ground deformation and shallow surface waves generated by Martian dust devils and perspectives for near-surface structure inversion. *Space Sci. Rev.* (2016, this issue)
- B.L.N. Kennett, The removal of free surface interactions from three component seismograms. *Geophys. J. Int.* **104**(1), 153–163 (1991)
- A. Khan, J. Connolly, Constraining the composition and thermal state of Mars from inversion of geophysical data. *J. Geophys. Res.* **113**(E07), 003 (2008). doi:[10.1029/2007JE002996](https://doi.org/10.1029/2007JE002996)
- A. Khan, K. Mosegaard, An inquiry into the lunar interior: a nonlinear inversion of the Apollo lunar seismic data. *J. Geophys. Res.* **107**, 5036 (2002). doi:[10.1029/2001JE001658](https://doi.org/10.1029/2001JE001658)
- A. Khan, K. Mosegaard, K.L. Rasmussen, A new seismic velocity model for the Moon from a Monte Carlo inversion of the Apollo lunar seismic data. *Geophys. Res. Lett.* **27**, 1591 (2000)
- A. Khan, J. Connolly, J. MacLennan, K. Mosegaard, Joint inversion of seismic and gravity data for lunar composition and thermal state. *Geophys. J. Int.* **168**, 243–258 (2007)
- A. Khan, L. Boschi, A. Connolly, On mantle chemical and thermal heterogeneities and anisotropy as mapped by inversion of global surface wave data. *J. Geophys. Res.* **114**(B09), 305 (2009). doi:[10.1029/2009JB006399](https://doi.org/10.1029/2009JB006399)
- A. Khan, A. Zunino, F. Deschamps, Upper mantle compositional variations and discontinuity topography imaged beneath Australia from bayesian inversion of surface-wave phase velocities and thermochemical modeling. *J. Geophys. Res.* **116** (2013). doi:[10.1002/jgrb.50304](https://doi.org/10.1002/jgrb.50304)
- A. Khan, J.A.D. Connolly, A. Pommier, J. Noir, Geophysical evidence for melt in the deep lunar interior and implications for lunar evolution. *J. Geophys. Res.* **119**, 2197–2221 (2014). doi:[10.1002/2014JE004661](https://doi.org/10.1002/2014JE004661)
- A. Khan, M. van Driel, M. Böse, D. Giardini, S. Ceylan, J. Yan, J. Clinton, F. Euchner, P. Lognonné, N. Murdoch, D. Mimoun, M.P. Panning, M. Knapmeyer, W.B. Banerdt, Single-station and single-event marsquake location and inversion for structure using synthetic Martian waveforms. *Phys. Earth Planet. Inter.* **258**, 28–42 (2016). doi:[10.1016/j.pepi.2016.05.017](https://doi.org/10.1016/j.pepi.2016.05.017)
- S. Kirkpatrick, C.D. Gelatt, M.P. Vecchi, Optimization by simulated annealing. *Science* **220**, 671–680 (1983). doi:[10.1126/science.220.4598.671](https://doi.org/10.1126/science.220.4598.671)
- M. Knapmeyer, Planetary seismology, in *Solar System, Landolt-Börnstein* ed. by J.E. Trümper. Group VI Astronomy and Astrophysics, vol. 4B (Springer, Berlin, 2009), pp. 282–322. Chap. 4.2.3
- M. Knapmeyer, Planetary core size: a seismological approach. *Planet. Space Sci.* **59**(10), 1062–1068 (2011)
- M. Knapmeyer, J. Oberst, E. Hauber, M. Wählisch, C. Deuchler, R. Wagner, Working models for spatial distribution and level of Mars' seismicity. *J. Geophys. Res.* **111**(E11), 006 (2006). doi:[10.1029/2006JE002708](https://doi.org/10.1029/2006JE002708)

- B. Knapmeyer-Endrun, M.P. Golombek, M. Ohrnberger, Rayleigh wave ellipticity modeling and inversion for shallow structure at the proposed InSight landing site in Elysium Planitia. *Mars. Space Sci. Rev.* (2016, this issue). doi:[10.1007/s11214-016-0300-1](https://doi.org/10.1007/s11214-016-0300-1)
- N. Kobayashi, K. Nishida, Continuous excitation of planetary free oscillations by atmospheric disturbances. *Nature* **395**, 357–360 (1998)
- J. Kolb, V. Lekić, Receiver function deconvolution using transdimensional hierarchical Bayesian inference. *Geophys. J. Int.* **197**(3), 1719–1735 (2014). doi:[10.1093/gji/ggu079](https://doi.org/10.1093/gji/ggu079)
- D. Komatitsch, J. Tromp, Spectral-element simulations of global seismic wave propagation—I. Validation. *Geophys. J. Int.* **149**, 390–412 (2002a). doi:[10.1046/j.1365-246X.2002.01653.x](https://doi.org/10.1046/j.1365-246X.2002.01653.x)
- D. Komatitsch, J. Tromp, Spectral-element simulations of global seismic wave propagation—II. 3-D models, oceans, rotation, self-gravitation. *Geophys. J. Int.* **150**, 303–318 (2002b). doi:[10.1046/j.1365-246X.2002.01716.x](https://doi.org/10.1046/j.1365-246X.2002.01716.x)
- A.S. Konopliv, R.S. Park, W.M. Folkner, An improved JPL Mars gravity field and orientation from Mars orbiter and lander tracking data. *Icarus* **274**, 253–260 (2016). doi:[10.1016/j.icarus.2016.02.052](https://doi.org/10.1016/j.icarus.2016.02.052)
- G.L. Kosarev, L.I. Makeyeva, L. Vinnik, Anisotropy of the mantle inferred from observations of P to S converted waves. *Geophys. J. R. Astron. Soc.* **76**, 209–220 (1984)
- C. Lachet, P.Y. Bard, Numerical and theoretical investigations on the possibilities and limitations of Nakamura's technique. *J. Phys. Earth* **42**, 377–397 (1994)
- D. Lammlein, G. Latham, J. Dorman, Y. Nakamura, M. Ewing, Lunar seismicity, structure and tectonics. *Rev. Geophys. Space Phys.* **12**, 1–21 (1974)
- C.A. Langston, Structure under Mount Rainier, Washington, inferred from teleseismic body waves. *J. Geophys. Res.* **84**(B9), 4749–4762 (1979)
- C. Larmat, J.P. Montagner, Y. Capdeville, W. Banerdt, P. Lognonné, J.P. Villette, Numerical assessment of the effects of topography and crustal thickness on Martian seismograms using a coupled modal solution–spectral element method. *Icarus* **196**(1), 78–89 (2008)
- E. Larose, A. Khan, Y. Nakamura, M. Campillo, Lunar subsurface investigated from correlation of seismic noise. *Geophys. Res. Lett.* **32**(L16), 201 (2005). doi:[10.1029/2005GL023518](https://doi.org/10.1029/2005GL023518)
- T. Lay, T. Wallace, *Modern Global Seismology* (Academic Press, San Diego, 1995)
- V. Lekić, J. Matas, M.P. Panning, B.A. Romanowicz, Measurement and implications of frequency dependence of attenuation. *Earth Planet. Sci. Lett.* **282**, 285–293 (2009). doi:[10.1016/j.epsl.2009.03.030](https://doi.org/10.1016/j.epsl.2009.03.030)
- J. Lermo, F. Chávez-García, Are microtremors useful in site response evaluation? *Bull. Seismol. Soc. Am.* **84**, 1350–1364 (1994)
- J.P. Ligorría, C.J. Ammon, Iterative deconvolution and receiver-function estimation. *Bull. Seismol. Soc. Am.* **89**(5), 1395–1400 (1999)
- V. Linkin, A.M. Harri, A. Lipatov, K. Belostotskaja, B. Derbunovich, A. Ekonomov, L. Khloustova, R. Kremnev, V. Makarov, B. Martinov, D. Nenarokov, M. Prostov, A. Pustovalov, G. Shustko, I. Järvinen, H. Kivilinna, S. Korpela, K. Kumpulainen, A. Lehto, R. Pellinen, R. Pirjola, P. Riihelä, A. Salminen, W. Schmidt, T. Siili, J. Blamont, T. Carpentier, A. Debus, C.T. Hua, J.F. Karczewski, H. Laplace, P. Levacher, P. Lognonné, C. Malique, M. Menyelle, G. Mouli, J.P. Pommereau, K. Quoth, J. Runavot, D. Vienne, F. Grunthaner, F. Kuhne, G. Musmann, R. Rieder, H. Wänke, T. Economou, M. Herring, A. Lane, C.P. McKay, A sophisticated lander for scientific exploration of Mars: scientific objectives and implementation of the Mars-96 Small Station. *Planet. Space Sci.* **46**, 717–737 (1998). doi:[10.1016/S0032-0633\(98\)00008-7](https://doi.org/10.1016/S0032-0633(98)00008-7)
- K. Lodders, B. Fegley, An oxygen isotope model for the composition of Mars. *Icarus* **126**, 373–394 (1997)
- P. Lognonné, C. Johnson, Planetary seismology, in *Treatise on Geophysics*, vol. 10, ed. by G. Schubert (Elsevier, Amsterdam, 2007), pp. 69–122
- P. Lognonné, C.L. Johnson, Planetary seismology, in *Treatise on Geophysics*, vol. 10, ed. by G. Schubert 2nd edn. (Elsevier, Oxford, 2015), pp. 65–120
- P. Lognonné, B. Mosser, Planetary seismology. *Surv. Geophys.* **14**, 239–302 (1993)
- P. Lognonné, W.T. Pike, Planetary seismometry, in *Extraterrestrial Seismology*, ed. by V.C.H. Tong, R. Garcia (Cambridge University Press, Cambridge, 2015), pp. 36–48. Chap. 3. doi:[10.1017/CBO9781107300668.006](https://doi.org/10.1017/CBO9781107300668.006)
- P. Lognonné, J.G. Beyneix, W.B. Banerdt, S. Cacho, J.F. Karczewski, M. Morand, Ultra broad band seismology on InterMarsNet. *Planet. Space Sci.* **44**, 1237 (1996). doi:[10.1016/S0032-0633\(96\)00083-9](https://doi.org/10.1016/S0032-0633(96)00083-9)
- P. Lognonné, E. Clévétré, H. Kanamori, Computation of seismograms and atmospheric oscillations by normal-mode summation for a spherical Earth model with realistic atmosphere. *Geophys. J. Int.* **135**, 388–406 (1998)
- P. Lognonné, D. Giardini, W. Banerdt, J. Gagnepain-Beyneix, A. Mocquet, T. Spohn, J. Karczewski, P. Schibler, S. Cacho, W. Pike, C. Cavoit, A. Desautez, M. Favède, T. Gabsi, L. Simoulin, N. Striebig, M. Campillo, A. Deschamp, J. Hinderer, J. Lévéque, J.P. Montagner, L. Rivéra, W. Benz, D. Breuer,

- P. Defraigne, V. Dehant, A. Fujimura, H. Mizutani, J. Oberst, The NetLander very broad band seismometer. *Planet. Space Sci.* **48**, 1289–1302 (2000)
- P. Lognonné, J. Gagnepain-Beyneix, W. Banerdt, H. Chenet, A new seismic model of the Moon: implication in terms of structure, formation, and evolution. *Earth Planet. Sci. Lett.* **211**, 27–44 (2003)
- P. Lognonné, M. Le Feuvre, C. Johnson, R.C. Weber, Moon meteoritic seismic hum: steady state prediction. *J. Geophys. Res.* **114**(E12), 003 (2009). doi:[10.1029/2008JE003294](https://doi.org/10.1029/2008JE003294)
- P. Lognonné, W.B. Banerdt, K. Hurst, D. Mimoun, R. Garcia, M. Lefevre, J. Gagnepain-Beyneix, M. Wieczorek, A. Mocquet, M. Panning, E. Beucler, S. Deraucourt, D. Giardini, L. Boschi, U. Christensen, W. Goetz, T. Pike, C. Johnson, R. Weber, K. Larmat, N. Kobayashi, J. Tromp, Insight and single-station broadband seismology: from signal and noise to interior structure determination, in *Lunar and Planetary Institute Science Conference Abstracts, Lunar and Planetary Institute Science Conference Abstracts*, vol. 43 (2012), p. 1983
- A.M. Lontsi, F.J. Sánchez-Sesma, J.C. Molina-Villegas, M. Ohrnberger, F. Krüger, Full microtremor H/V(z, f) inversion for shallow subsurface characterization. *Geophys. J. Int.* **202**, 298–312 (2015). doi:[10.1093/gji/ggv132](https://doi.org/10.1093/gji/ggv132)
- M.C. Malin, K.S. Edgett, L.V. Posiolova, S.M. McColley, E.Z.N. Dobrea, Present-day impact cratering rate and contemporary gully activity on Mars. *Science* **314**, 1573–1577 (2006)
- P. Malischewsky, F. Scherbaum, Love's formula and H/V ratio (ellipticity) of Rayleigh waves. *Wave Motion* **40**, 57–67 (2004). doi:[10.1016/j.wavemoti.2003.12.015](https://doi.org/10.1016/j.wavemoti.2003.12.015)
- K. Matsumoto, R. Yamada, F. Kikuchi, S. Kamata, Y. Ishihara, T. Iwata, H. Hanada, S. Sasaki, Internal structure of the Moon inferred from Apollo seismic data and selenodetic data from GRAIL and LLR. *Geophys. Res. Lett.* **42**, 7351–7358 (2015). doi:[10.1002/2015GL065335](https://doi.org/10.1002/2015GL065335)
- H. McSween, What we have learned about Mars from SNC meteorites. *Meteoritics* **29**, 757–779 (1994)
- N. Metropolis, A. Rosenbluth, M. Rosenbluth, A. Teller, E. Teller, Equation of state calculations by fast computing machines. *J. Chem. Phys.* **21**, 1087–1091 (1953)
- D. Mimoun, P. Lognonné, W.B. Banerdt, K. Hurst, S. Deraucourt, J. Gagnepain-Beyneix, T. Pike, S. Calcutt, M. Bierwirth, R. Roll, P. Zweifel, D. Mance, O. Robert, T. Nébut, S. Tillier, P. Laudet, L. Kerjean, R. Perez, D. Giardini, U. Christensen, R. Garcia, The InSight SEIS experiment, in *Lunar and Planetary Institute Science Conference Abstracts, Lunar and Planetary Institute Science Conference Abstracts*, vol. 43 (2012), p. 1493
- D. Mimoun, N. Murdoch, P. Lognonné, W.T. Pike, K. Hurst (the SEIS Team), The seismic noise model of the InSight mission to Mars. *Space Sci. Rev.* (2016, this issue)
- A. Mocquet, P. Vacher, O. Grasset, C. Sotin, Theoretical seismic models of Mars: the importance of the iron content of the mantle. *Planet. Space Sci.* **44**, 1251–1268 (1996)
- R.K. Mohapatra, S.V.S. Murty, Precursors of Mars—constraints from nitrogen and oxygen isotopic compositions of martian meteorites. *Meteorit. Planet. Sci.* **38**, 225–242 (2003)
- J.W. Morgan, E. Anders, Chemical composition of Mars. *EOS Trans AGU* 60:306 (1979)
- K. Mosegaard, A. Tarantola, Monte-Carlo sampling of solutions to inverse problems. *J. Geophys. Res.* **100**, 12431–12447 (1995)
- N. Murdoch, D. Mimoun, P. Lognonné (SEIS Science Team), SEIS performance model environment document. *Tech. Rep. ISGH-SEIS-JF-ISAE-0030*, ISAE (2015)
- N. Murdoch, B. Kenda, T. Kawamura, A. Spiga, P. Lognonné, D. Mimoun, W.B. Banerdt, Estimations of the seismic pressure noise on Mars determined from Large Eddy Simulations and demonstration of pressure decorrelation techniques for the InSight mission. *Space Sci. Rev.* (2016a, this issue)
- N. Murdoch, D. Mimoun, R.F. Garcia, W. Rapin, T. Kawamura, P. Lognonné, Evaluating the wind-induced mechanical noise on the InSight seismometers. *Space Sci. Rev.* (2016b, this issue)
- Y. Nakamura, Seismic velocity structure of the lunar mantle. *J. Geophys. Res.* **88**, 677–686 (1983)
- Y. Nakamura, A method for dynamic characteristics estimation of subsurface using microtremor on the ground surface. *Q. Rep. RTRI* **30**, 25–33 (1989)
- Y. Nakamura, Clear identification of fundamental idea of Nakamura's technique and its applications, in *Proceedings of the 12th World Conference on Earthquake Engineering*, Auckland (2000)
- Y. Nakamura, Farside deep moonquakes and deep interior of the Moon. *J. Geophys. Res.* **110**(E01), 001 (2005). doi:[10.1029/2004JE002332](https://doi.org/10.1029/2004JE002332)
- Y. Nakamura, On the H/V spectrum, in *Proceedings of the 14th World Conference on Earthquake Engineering*, Beijing (2008)
- Y. Nakamura, D. Anderson, Martian wind activity detected by a seismometer at Viking Lander 2 site. *Geophys. Res. Lett.* **6**, 499–502 (1979). doi:[10.1029/GL006i006p00499](https://doi.org/10.1029/GL006i006p00499)
- Y. Nakamura, J. Dorman, F. Duennebier, D. Lammlein, G. Latham, Shallow lunar structure determined from the passive seismic experiment. *Moon* **13**, 57–66 (1975)

- Y. Nakamura, G. Latham, H. Dorman, A.B. Ibrahim, J. Koyama, P. Horvarth, Shallow moonquakes—depth, distribution and implications as to the present state of the lunar interior, in *Proc. Lunar Planet. Sci. Conf.*, vol. 10 (1979), pp. 2299–2309
- G. Neumann, M. Zuber, M. Wieczorek, P. McGovern, F. Lemoine, D. Smith, Crustal structure of Mars from gravity and topography. *J. Geophys. Res.* **109**(E8), 002 (2004). doi:[10.1029/2004JE002262](https://doi.org/10.1029/2004JE002262)
- F. Nimmo, U.H. Faul, Dissipation at tidal and seismic frequencies in a melt-free, anhydrous Mars. *J. Geophys. Res.* **118**(12), 2558–2569 (2013). <http://dx.doi.org/10.1002/2013JE004499>. doi:[10.1002/2013JE004499](https://doi.org/10.1002/2013JE004499)
- Nishikawa et al., Title to be completed. *Space Sci. Rev.* (2016, this issue)
- T. Nissen-Meyer, M. van Driel, S.C. Stähler, K. Hosseini, S. Hempel, L. Auer, A. Colombi, A. Fournier, AxiSEM: broadband 3-D seismic wavefields in axisymmetric media. *Solid Earth* **5**(1), 425–445 (2014)
- E.A. Okal, D.L. Anderson, Theoretical models for Mars and their seismic properties. *Icarus* **33**, 514–528 (1978). doi:[10.1016/0019-1035\(78\)90187-2](https://doi.org/10.1016/0019-1035(78)90187-2)
- R.D. Oldham, The constitution of the interior of the Earth, as revealed by earthquakes. *Q. J. Geol. Soc. Lond.* **62**(1–4), 456–475 (1906)
- M.P. Panning, E. Beucler, M. Drilleau, A. Mocquet, P. Lognonné, W.B. Banerdt, Verifying single-station seismic approaches using Earth-based data: Preparation for data return from the InSight mission to Mars. *Icarus* **248**, 230–242 (2015). doi:[10.1016/j.icarus.2014.10.035](https://doi.org/10.1016/j.icarus.2014.10.035)
- A. Panou, N. Theodoulidis, P. Hatzidimitriou, K. Stylianidis, C. Papazachos, Ambient noise horizontal-to-vertical spectral ratio in site effects estimation and correlation with seismic damage distribution in urban environment: the case of the city of Thessaloniki (Northern Greece). *Soil Dyn. Earthq. Eng.* **25**, 261–274 (2005). doi:[10.1016/j.soildyn.2005.02.004](https://doi.org/10.1016/j.soildyn.2005.02.004)
- J. Park, V. Levin, Receiver functions from multiple-taper spectral correlation estimates. *Bull. Seismol. Soc. Am.* **90**(6), 1507–1520 (2000)
- J. Park, C.R. Lindberg, D.J. Thomson, Multiple-taper spectral analysis of terrestrial free oscillations: part I. *Geophys. J. Int.* **91**(3), 755–794 (1987). doi:[10.1111/j.1365-246X.1987.tb01668.x](https://doi.org/10.1111/j.1365-246X.1987.tb01668.x)
- R. Phillips, Expected rate of marsquakes, in *Scientific Rationale and Requirements for a Global Seismic Network on Mars* (1991), pp. 35–38. LPI Tech. Rept., 91-02, Lunar and Planetary Inst., Houston
- A. Pivarunas, N.H. Warner, M.P. Golombek, Onset diameter of rocky ejecta craters in western Elysium Planitia, Mars: constraints for regolith thickness at the InSight landing site, in *46th Lunar and Planetary Science Conference, Lunar and Planetary Inst.*, Houston, TX (2015). p Abstract # 1129. <http://www.hou.usra.edu/meetings/lpsc2015/pdf/1129.pdf>
- A.C. Plesa, M. Grott, N. Tosi, D. Breuer, T. Spohn, M. Wieczorek, How large are present-day heat flux variations across the surface of Mars? *J. Geophys. Res.* (2016, accepted). doi:[10.1002/2016JE005126](https://doi.org/10.1002/2016JE005126)
- J.B. Plescia, Recent flood lavas in the Elysium region of Mars. *Icarus* **88**, 465–490 (1990)
- V. Poggi, D. Fäh, J. Burjanek, D. Giardini, The use of Rayleigh-wave ellipticity for site-specific hazard assessment and microzonation: application to the city of Lucerne, Switzerland. *Geophys. J. Int.* **188**, 1154–1172 (2012). doi:[10.1111/j.1365-246X.2011.05305.x](https://doi.org/10.1111/j.1365-246X.2011.05305.x)
- F. Press, Earth models obtained by Monte Carlo inversion. *J. Geophys. Res.* **73**, 5223–5234 (1968). doi:[10.1029/JB073i016p05223](https://doi.org/10.1029/JB073i016p05223)
- D.A. Quiros, L.D. Brown, D. Kim, Seismic interferometry of railroad induced ground motions: body and surface wave imaging. *Geophys. J. Int.* **205**, 301–313 (2016). doi:[10.1093/gji/ggw033](https://doi.org/10.1093/gji/ggw033)
- J.E. Richardson, H.J. Melosh, R.J. Greenberg, D.P. O'Brien, The global effects of impact-induced seismic activity on fractured asteroid surface morphology. *Icarus* **179**, 325–349 (2005)
- A. Rivoldini, T. Van Hoolst, The interior structure of Mercury constrained by the low-degree gravity field and the rotation of Mercury. *Earth Planet. Sci. Lett.* **377–378**, 67–72 (2013). doi:[10.1016/j.epsl.2013.07.021](https://doi.org/10.1016/j.epsl.2013.07.021)
- A. Rivoldini, T. Van Hoolst, O. Verhoeven, A. Mocquet, V. Dehant, Geodesy constraints on the interior structure and composition of Mars. *Icarus* **213**, 451–472 (2011)
- G.P. Roberts, B. Matthews, C. Bristow, L. Guerrieri, J. Vetterlein, Possible evidence of paleomarsquakes from fallen boulder populations, Cerberus Fossae, Mars. *J. Geophys. Res.* **117**(E003), 816 (2012)
- S. Rost, C. Thomas, Improving seismic resolution through array processing techniques. *Surv. Geophys.* **30**, 271–299 (2009)
- M. Sambridge, Geophysical inversion with a neighbourhood algorithm—I. searching a parameter space. *Geophys. J. Int.* **138**, 479–494 (1999). doi:[10.1046/j.1365-246X.19993.00876.x](https://doi.org/10.1046/j.1365-246X.19993.00876.x)
- F.J. Sánchez-Sesma, C.B. Crouse, Effects of site geology on seismic ground motion: Early history. *Earthq. Eng. Struct. Dyn.* **44**, 1099–1113 (2015). doi:[10.1002/eqe.2503](https://doi.org/10.1002/eqe.2503)
- F.J. Sánchez-Sesma, M. Rodríguez, U. Iturrarán-Viveros, F. Luzón, M. Campillo, L. Margerin, A. García-Jerez, M. Suárez, M.A. Santoyo, A. Rodríguez-Castellanos, A theory for microtremor H/V spectral ratio: application for a layered medium. *Geophys. J. Int.* **186**, 221–225 (2011). doi:[10.1111/j.1365-246X.2011.05064.x](https://doi.org/10.1111/j.1365-246X.2011.05064.x)

- C. Sanloup, A. Jambon, P. Gillet, A simple chondritic model of Mars. *Phys. Earth Planet. Inter.* **112**, 43–54 (1999)
- F. Scherbaum, K.G. Hinzen, M. Ohrnberger, Determination of shallow shear wave velocity profiles in the Cologne, Germany area using ambient vibrations. *Geophys. J. Int.* **152**, 597–612 (2003). doi:[10.1046/j.1365-246X.2003.01856.x](https://doi.org/10.1046/j.1365-246X.2003.01856.x)
- N.C. Schmerr, B.M. Kelly, M.S. Thorne, Broadband array observations of the 300 km seismic discontinuity. *Geophys. Res. Lett.* **40**(5), 841–846 (2013)
- J. Schweitzer, J. Fyen, S. Mykkeltveit, T. Kværna, Seismic arrays, in *IASPEI New Manual of Seismological Observatory Practice*, ed. by P. Bormann (2002). GFZ German Research Center for Geosciences, Potsdam
- N. Shapiro, M. Ritzwoller, Monte-Carlo inversion for a global shear-velocity model of the crust and upper mantle. *Geophys. J. Int.* **151**, 88–105 (2002)
- P. Shearer, *Introduction to Seismology* (Cambridge University Press, Cambridge, 2009)
- F. Sohl, T. Spohn, The interior structure of Mars: implications from SNC meteorites. *J. Geophys. Res.* **102**(E1), 1613–1635 (1997)
- T. Spohn, M. Grott, S. Smrekar, C. Krause, T.L. Hudson (the HP<sup>3</sup> instrument team), Measuring the martian heat flow using the heat flow and physical properties package (HP<sup>3</sup>), in *45th Lunar and Planetary Science Conference, Lunar and Planetary Inst.*, Houston, TX (2014). <http://www.hou.usra.edu/meetings/lpsc2014/pdf/1916.pdf>
- B. Steinberger, D. Zhao, S.C. Werner, Interior structure of the Moon: constraints from seismic tomography, gravity and topography. *Phys. Earth Planet. Inter.* **245**, 26–39 (2015). doi:[10.1016/j.pepi.2015.05.005](https://doi.org/10.1016/j.pepi.2015.05.005)
- L. Stixrude, C. Lithgow-Bertelloni, Thermodynamics of mantle minerals—II. phase equilibria. *Geophys. J. Int.* **184**(3), 1180–1213 (2011). doi:[10.1111/j.1365-246X.2010.04890.x](https://doi.org/10.1111/j.1365-246X.2010.04890.x)
- R. Takashi, K. Hirano, Seismic vibrations of soft ground (in Japanese). *Bull. Earthq. Res. Inst. Univ. Tokyo* **19**, 534–543 (1941)
- T. Tanimoto, L. Rivera, The zh ratio method for long-period seismic data: sensitivity kernels and observational techniques. *Geophys. J. Int.* **172**(1), 214–219 (2008)
- T. Tanimoto, M. Eitzel, T. Yano, The noise cross-correlation approach for Apollo 17 LPSE data: Diurnal change in seismic parameters in the shallow lunar crust. *J. Geophys. Res.* **113**(E08), 011 (2008). doi:[10.1029/2007JE003016](https://doi.org/10.1029/2007JE003016)
- G.J. Taylor, The bulk composition of Mars. *Chemie der Erde. Geochem.* **73**(4), 401–420 (2013). doi:[10.1016/j.chemer.2013.09.006](https://doi.org/10.1016/j.chemer.2013.09.006)
- J. Taylor, N.A. Teanby, J. Wookey, Estimates of seismic activity in the Cerberus Fossae region of Mars. *J. Geophys. Res.* **E118**, 2570–2581 (2013)
- N.A. Teanby, Predicted detection rates of regional-scale meteorite impacts on Mars with the InSight short-period seismometer. *Icarus* **256**, 49–62 (2015)
- N.A. Teanby, J. Wookey, Seismic detection of meteorite impacts on Mars. *Phys. Earth Planet. Inter.* **186**, 70–80 (2011)
- N.A. Teanby, J. Stevanović, J. Wookey, N. Murdoch, J. Hurley, R. Myhill, N.E. Bowles, S.B. Calcutt, W.T. Pike, Seismic coupling of short-period wind noise through Mars' regolith for NASA's InSight lander. *Space Sci. Rev.* (2016, this issue)
- W. Thomson, On the rigidity of the Earth. *Philos. Trans. R. Soc. Lond.* **153**, 573–582 (1863). doi:[10.1098/rstl.1863.0027](https://doi.org/10.1098/rstl.1863.0027)
- T. Van Hoolst, V. Dehant, F. Roosbeek, P. Lognonné, Tidally induced surface displacements, external potential variations, and gravity variations on Mars. *Icarus* **161**(2), 281–296 (2003). doi:[10.1016/S0019-1035\(02\)00045-3](https://doi.org/10.1016/S0019-1035(02)00045-3)
- J.D. Vaucher, D. Baratoux, N. Mangold, P. Pinet, K. Kurita, M. Grégoire, The volcanic history of central Elysium Planitia: implications for martian magmatism. *Icarus* **204**, 418–442 (2009)
- O. Verhoeven, A. Rivoldini, P. Vacher, A. Mocquet, G. Choblet, M. Menville, V. Dehant, T. Van Hoolst, J. Sleewaegen, J.P. Barriot, P. Lognonné, Interior structure of terrestrial planets: modeling Mars' mantle and its electromagnetic, geodetic, and seismic properties. *J. Geophys. Res.* **110**(E04), 009 (2005). doi:[10.1029/2004JE002271](https://doi.org/10.1029/2004JE002271)
- J. Vetterlein, G.P. Roberts, Structural evolution of the Northern Cerberus Fossae graben system, Elysium Planitia, Mars. *J. Struct. Geol.* **32**, 394–406 (2010). doi:[10.1016/j.jsg.2009.11.004](https://doi.org/10.1016/j.jsg.2009.11.004)
- S. Vinciguerra, C. Trovato, P.G. Meredith, P.M. Benson, Relating seismic velocities, thermal cracking and permeability in Mt. Etna and Iceland basalts. *Int. J. Rock Mech. Min. Sci.* **42**, 900–910 (2005). doi:[10.1016/j.ijrmms.2005.05.022](https://doi.org/10.1016/j.ijrmms.2005.05.022)
- L. Vinnik, H. Chenet, J. Gagnepain-Beyneix, P. Lognonné, First seismic receiver functions on the Moon. *Geophys. Res. Lett.* **28**, 3031–3034 (2001)
- E. Von Rebeur-Paschwitz, The earthquake of Tokio 18 April 1889. *Nature* **40**, 294–295 (1889). doi:[10.1038/040294e0](https://doi.org/10.1038/040294e0)

- N. Warner, M.P. Golombek, J. Sweeney, R. Fergason, R. Kirk, C. Schwartz, Near surface stratigraphy and regolith production in southwestern Elysium Planitia, Mars: Implications of Hesperian-Amazonian terrains and the InSight lander mission. *Space Sci. Rev.* (2016, this issue)
- M. Wathelet, An improved neighborhood algorithm: parameter conditions and dynamic scaling. *Geophys. Res. Lett.* **35**(L09), 301 (2008). doi:[10.1046/j.1365-246X.1999.00876.x](https://doi.org/10.1046/j.1365-246X.1999.00876.x)
- M. Wathelet, D. Jongmans, M. Ohrnberger, Surface-wave inversion using a direct search algorithm and its application to ambient vibration measurements. *Near Surf. Geophys.* **2**, 211–221 (2004)
- R. Weber, P.Y. Lin, E. Garnero, Q. Williams, P. Lognonné, Seismic detection of the lunar core. *Science* **331**(6015), 309–312 (2011)
- S.G. Wells, J.C. Dohrenwend, L.D. McFadden, B.D. Turrin, K.D. Mahrer, Late Cenozoic landscape evolution on lava flow surfaces of the Cima volcanic field, Mojave Desert, California. *Geol. Soc. Am. Bull.* **96**, 1518–1529 (1985)
- M. Wieczorek, M. Zuber, Thickness of the Martian crust: Improved constraints from geoid-to-topography ratios. *J. Geophys. Res.* **109**(E01), 009 (2004). doi:[10.1029/2003JE002153](https://doi.org/10.1029/2003JE002153)
- D.R. Williams (2016). <http://nssdc.gsfc.nasa.gov/planetary/factsheet/marsfact.html>
- J.P. Williams, A.V. Pathare, O. Aharonson, The production of small primary craters on Mars and the Moon. *Icarus* **235**, 23–36 (2014)
- J. Woodhouse, The calculation of eigenfrequencies and eigenfunctions of the free oscillations of the Earth and the Sun, in *Seismological Algorithms*, ed. by D. Doornbos (Academic Press, London, 1988), pp. 321–370
- D. Zhao, T. Arai, L. Liu, E. Ohtani, Seismic tomography and geochemical evidence for lunar mantle heterogeneity: comparing with Earth. *Glob. Planet. Change* **90**, 29–36 (2012). doi:[10.1016/j.gloplacha.2012.01.004](https://doi.org/10.1016/j.gloplacha.2012.01.004)
- V.N. Zharkov, T.V. Gudkova, On the dissipative factor of the martian interiors. *Planet. Space Sci.* **45**, 401–407 (1997)
- V.N. Zharkov, T.V. Gudkova, S.M. Molodensky, On models of Mars' interior and amplitudes of forced nutations: 1. the effects of deviation of Mars from its equilibrium state on the flattening of the core–mantle boundary. *Phys. Earth Planet. Inter.* **172**, 324–334 (2009). doi:[10.1016/j.pepi.2008.10.009](https://doi.org/10.1016/j.pepi.2008.10.009)
- Y. Zheng, F. Nimmo, T. Lay, Seismological implications of a lithospheric low seismic velocity zone in Mars. *Phys. Earth Planet. Inter.* **240**, 132–141 (2015). doi:[10.1016/j.pepi.2014.10.004](https://doi.org/10.1016/j.pepi.2014.10.004)